

Unified Timing Analysis for Closed-Loop Goal-Oriented Wireless Communication

Lintao Li, Anders E. Kalør, *Member, IEEE*, Petar Popovski, *Fellow, IEEE*, and Wei Chen, *Senior Member, IEEE*

Abstract—Goal-oriented communication has become one of the focal concepts in sixth-generation communication systems owing to its potential to provide intelligent, immersive, and real-time mobile services. The emerging paradigms of goal-oriented communication constitute closed loops integrating communication, computation, and sensing. However, challenges arise for closed-loop timing analysis due to multiple random factors that affect the communication/computation latency, as well as the heterogeneity of feedback mechanisms across multi-modal sensing data. To tackle these problems, we aim to provide a unified timing analysis framework for closed-loop goal-oriented communication (CGC) systems over fading channels. The proposed framework is unified as it considers computation, compression, and communication latency in the loop with different configurations. To capture the heterogeneity across multi-modal feedback, we categorize the sensory data into the periodic-feedback and event-triggered, respectively. We formulate timing constraints based on average and tail performance, covering timeliness, jitter, and reliability of CGC systems. A method based on saddlepoint approximation is proposed to obtain the distribution of closed-loop latency. The results show that the modified saddlepoint approximation is capable of accurately characterizing the latency distribution of the loop with analytically tractable expressions. This sets the basis for low-complexity co-design of communication and computation.

Index Terms—closed-loop timing analysis, multi-modal feedback, immersive communication, saddlepoint approximation.

I. INTRODUCTION

A. Motivation and Contributions

Driven by the rapid development of information technology and the continuous improvement of hardware capability, the sixth-generation (6G) communication systems are envisioned to fuse the physical and digital worlds by providing intelligent, immersive, and real-time services [1]. This is, for

The work of Lintao Li and Wei Chen was supported by the National Natural Science Foundation of China/Research Grants Council Collaborative Research Scheme under Grant No. 62261160390. The work of A. E. Kalør was supported in part by the Independent Research Fund Denmark (IRFD) under Grant 1056-00006B and in part by the Horizon Europe SNS project “6G-GOALS” (grant 101139232). The work of P. Popovski was supported in part by the Villum Investigator Grant “WATER” from the Velux Foundation, Denmark, and in part by the Horizon Europe SNS project “6G-GOALS” (grant 101139232).

Lintao Li and Wei Chen are with the Department of Electronic Engineering, Tsinghua University, Beijing 100084, China, and also with the Beijing National Research Center for Information Science and Technology, Tsinghua University, Beijing 100084, China (email: llt20@mails.tsinghua.edu.cn; wchen@tsinghua.edu.cn).

Anders E. Kalør is with the Department of Information and Computer Science, Keio University, Yokohama 223-8522, Japan, and with the Department of Electronic Systems, Aalborg University, 9220 Aalborg, Denmark (e-mail: aek@keio.jp).

Petar Popovski is with the Department of Electronic Systems, Aalborg University, 9220 Aalborg, Denmark (e-mail: petarp@es.aau.dk).

instance, reflected in the IMT-2030 draft for the 6G wireless communication technology [2] published by the International Telecommunication Union (ITU), which in addition to hyper reliable and low-latency communication also includes immersive communication as central 6G usage scenarios. Against this background, the goal-oriented communication paradigm gets significant traction in 6G [3]. Supported by artificial intelligence (AI), goal-oriented communication aims to provide intelligent and immersive experiences for users by optimizing the communication for the receiver’s intention and experience, rather than simply providing reliable, content-blind packet delivery [4], [5]. Combined with Metaverse and Digital Twin (DT) technology, this enables 6G to break the spatial constraints to promote the achievement of the flexible interconnection between the physical world and the digital virtual space [6].

Differently from 5G, goal-oriented paradigms require demanding *closed-loop* interactions with strict timing requirements, starting from the commands transmitted by the user and ending with the reception of feedback. The closed-loop interactions are common in several of the typical 6G scenarios considered by the Third Generation Partnership Project (3GPP) [7], including remote control, virtual social, and gaming. However, the closed-loop timing analysis is challenging compared to the point-to-point perspective that has dominated the literature so far, as it needs to consider processing latency of intermediate notes caused by, e.g., compression and computation. Thus, there is a need to develop a unified timing-analysis framework for closed-loop goal-oriented communication (CGC) systems over wireless channels, which can serve as a tool to ensure that users get the desired real-time experience.

To address this issue, we aim to formulate a unified framework for timing analysis in CGC systems, accounting for communication, computation, and compression latency. Specifically, we consider a general CGC system, comprising a user equipment (UE), a base station (BS), and a remote agent (RA), all assumed to operate in a closed loop. The system is exemplified as a robotic scenario with a DT at the BS in Fig. 1. We consider both periodic and sporadic traffic. The periodic traffic, referred to as periodic feedback (PF), is transmitted at fixed intervals from the RA to UE, representing, e.g., sensor data. The sporadic traffic is initiated by control data sent from the UE to RA, which then responds with event-triggered (ET) data. Communication occurs through the BS, which is equipped with a mobile-edge-computing (MEC) server to handle computation tasks, such as feature extraction, compression, and decompression. Although the remote agent is depicted as a robot, it could also function as a cloud server in

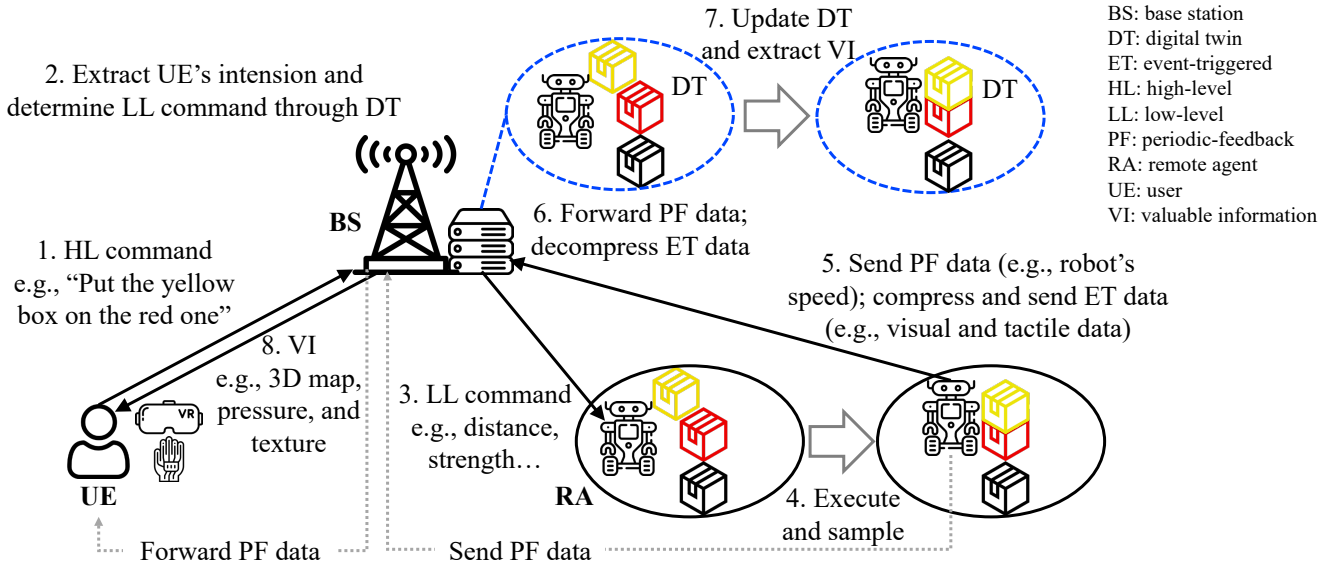


Fig. 1. System model for a general CGC system. This figure shows an example of the remote control with the assistance of MEC, semantic information, and DT. Multiple communication and computation processes are included in this closed loop.

a gaming scenario or as another UE in a virtual social scenario. A key novelty of the proposed model is its capability to enable closed-loop analysis of heterogeneous multi-modal feedback, comprising both event-triggered and periodic feedback, along with stochastic computation and compression latency. In goal-oriented systems with various goals, such as metaverse systems that ensure an immersive experience for UEs, these elements are generally present. The stochastic nature of the computation and compression latency has been ignored in most existing work, although they are crucial for end-to-end latency analysis [8]–[10]. Besides, motivated by perceptual requirements of interactive applications [7], [11]–[13], we explicitly model the asynchrony between the transmission latency of PF and ET data, referred to as *jitter*. Further details of the model will be given in Section II.

Note that the model in Fig. 1 is rather general, capable to cover some commonly referred scenarios for CGC systems. For the remote control task shown in Fig. 1, we are interested in the closed-loop latency by accounting for the timeliness of the control data and the jitter of the multi-modal feedback. For the authorization of avatar usage rights, specified by 3GPP in [7], the RA acts as a cloud server. UE sends requests to the cloud server through BS without relying on the computation process at the BS. Once the cloud server receives the requests, it inquires and returns profiles of the avatar to the UE. Meanwhile, authorization information will be sent to UE periodically to authorize the use of the avatar legally. In this scenario, reducing the asynchrony between profile reception and authorization ensures immediate avatar utilization without additional latency. Differently from the remote control, we focus on the closed-loop latency without a specific concern of control link latency.

Using the proposed model, and with consideration of timeliness, jitter, and reliability, we formulate a unified framework of timing analysis for CGC systems, capable of addressing both

average- and tail-based timing constraints for CGC systems with different information-processing mechanisms and configurations. To this end, we propose a general saddlepoint-approximation-based method to obtain the analytical expression of the distribution of closed-loop latency with high accuracy. Then a low-complexity joint SPA and CLT-based approximation method is proposed. Based on the joint SPA and CLT-based approximation method, we also give a corollary for efficiently approximating the conditional expectation given the timing constraints. The proposed methods can be generalized to timing analysis in other closed-loop scenarios.

The main contributions are summarized as follows:

- We formulate a unified timing-analysis framework for CGC systems with different configurations, which takes the randomness of the computation, compression, and communication latency into account. The formulated framework integrates the timeliness, jitter, and reliability of CGC systems.
- We consider two heterogeneous information flows with both PF and ET data, representing different feedback mechanisms of multi-modal sensing data.
- We propose a general saddlepoint approximation (SPA)-based method for analytically characterizing the timing measures in CGC systems. For specific scenarios, the central limit theorem (CLT) is also utilized to improve the efficiency of the method while ensuring accuracy.
- Based on the joint SPA and CLT-based approximation, an efficient approximation is presented for calculating the conditional expectation given timing constraints.

B. Related Work

In [16], a goal-oriented communication and prediction co-design was proposed to improve the reliability of the haptic communication system. The end-to-end communication latency was chosen as the timing metric with a queueing model,

TABLE I
COMPARISON WITH RELATED WORKS

Work	Computation Time	Feedback Mechanism	Analyzing Method	Considered Scenarios
[14]	Not consider	Event-triggered	Queueing theory	Remote control
[15]	Deterministic	Event-triggered	SPA for i.i.d. random variables	Federated learning
[8]	Stochastic	Event-triggered	Truncated convolution	Remote control
This work	Stochastic	Event-triggered, periodic	SPA for non-i.i.d. random variables	General CGC systems

TABLE II
ACRONYMS USED IN THE PAPER

Abbreviation	Definition
CGC	closed-loop goal-oriented communication
DT	digital twin
AI	artificial intelligence
UE	user equipment
BS	base station
RA	remote agent
PF	periodic feedback
ET	event-triggered
MEC	mobile edge computing
CLT	central limit theorem
SPA	saddlepoint approximation
CDF	cumulative distribution function
PDF	probability density function
PMF	probability mass function
FL	feedback link
CL	control link
VI	valuable information
FSD	frequency or spatial diversity
HL	high-level
LL	low-level
CD	compressed data
SNR	signal-to-noise ratio
CSIRT	channel state information known at both receiver and transmitter

while the computation latency is omitted in [16]. Wen *et al.* optimized the discriminant gain to achieve the goal of improving the accuracy of AI inference in an integrated sensing and communication system [17]. Meanwhile, they considered the latency constraint in this system, which focused on the uplink latency comprised of communication, computation, and sensing procedures. The authors of [18] designed resource allocation and computation offloading schemes to minimize the uplink latency of DT-enabled Metaverse. In [17] and [18], the constant computation latency is incorporated into the timing measurements. However, they only considered the one-way latency instead of the closed-loop latency.

Conducting closed-loop timing analysis was proved to be effective for the wireless networked control system in [19] and [14]. Thus, it is important to analyze the timing performance of a goal-oriented communication system from the closed-loop perspective. In [15], the authors carried out the closed-loop timing analysis for wireless federated learning systems by taking both random latency of local information uploading and global model broadcasting into account. However, the computation latency was also assumed as a deterministic term in

[15], which ignored its stochastic property [8]–[10]. To address these problems, Suman *et al.* conducted a statistical timing analysis for a closed-loop teleoperation system [8], in which the randomness of computation and compression latency were accounted for. However, the heterogeneity between the multi-modal feedback, which widely exists in various goal-oriented communication, was not considered.

The SPA technique that we apply is a powerful method to approximate complicated distributions with high accuracy guarantees while avoiding intractable computations [20]. SPA has been widely used in communication research. In [15], SPA was used to characterize the distribution of transmission latency in wireless federated learning systems. An efficient SPA-based method for evaluating block error probabilities was proposed in [21], and the power-latency-throughput tradeoff of delay-constrained wireless systems was characterized by SPA in [22].

C. Paper Organization and Notation

The paper is structured as follows. Section II presents the unified timing framework for CGC systems considered in this paper. Section III introduces the latency components and formally defines the overall objective, while Section IV proposes the SPA-based timing analysis for the CGC system. Section V validates the analysis through numerical results, and finally the paper is concluded in Section VI.

Notation: $\mathbb{E}\{x\}$ denotes the expectation of the random variable x , and $\text{Var}\{x\}$ denotes its variance. $f'(x)$ and $f''(x)$ denote the first-order and second-order derivative of $f(x)$, respectively. $\mathcal{N}(0, 1)$ denotes the standard Gaussian distribution with cumulative distribution function (CDF) $\Phi(x) = \frac{1}{\sqrt{2\pi}} \int_{-\infty}^x e^{-\frac{y^2}{2}} dy$ and probability density function (PDF) $\phi(x) = \frac{1}{\sqrt{2\pi}} e^{-\frac{x^2}{2}}$. $\gamma(s, x) = \int_0^x t^{s-1} e^{-t} dt$ is the lower incomplete gamma function, $\{x\}^+ = \max\{x, 0\}$, and $\text{sign}(x)$ denotes the sign of x .

II. A UNIFIED FRAMEWORK FOR TIMING ANALYSIS IN CGC SYSTEMS WITH DIFFERENT CONFIGURATIONS

In this section, we present a unified framework for timing analysis in CGC systems. We begin by providing an overview of the system, followed by an introduction to latency components. Section II-C outlines the wireless channel model, while Section II-D specifies different timing constraints employed to formulate the proposed framework with diverse configurations.

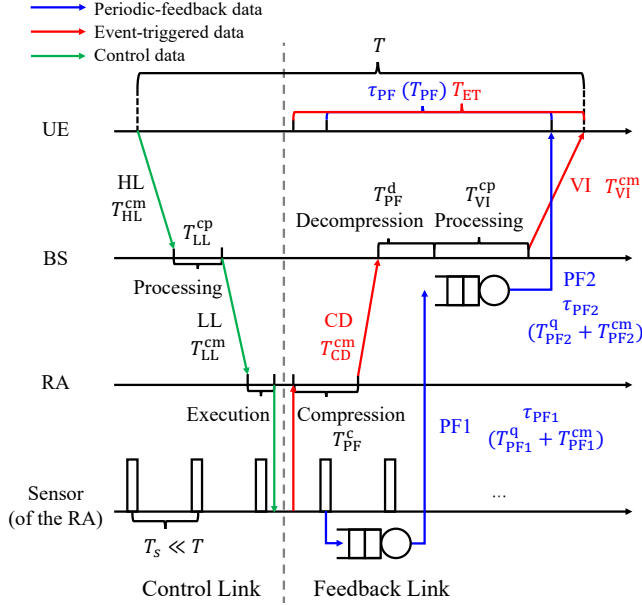


Fig. 2. Diagram of the components of the closed-loop latency. The UE transmits commands to the RA through the control link, and the RA transmits both periodic-feedback and event-triggered sensor data to the UE.

A. System Overview

We study the CGC system illustrated in Fig. 1, which comprises a BS, a UE, and a RA equipped with a sensor. The UE and the RA communicate over a wireless channel via the BS, using dedicated channel resources. Additionally, the BS is equipped with an MEC server to perform computation tasks, including feature extraction and decompression. We designate the channel from the UE to the RA as the *control link* (CL), while the link from the RA to the UE is the *feedback link* (FL). The communication flow is depicted in Fig. 2, where we consider three types of data: control data, periodic-feedback (PF) data, and event-triggered (ET) data.

Control data is transmitted sporadically by the UE as high-level (HL) commands, assumed to be sent at relatively long intervals to eliminate the need for queuing. For instance, control data may represent the UE's intention to place the yellow box on the red one, as shown in Fig. 1. The HL commands are subject to a random processing delay at the BS. Specifically, the UE transmits an HL command to the BS, which then processes the received command to extract the semantic information, for instance, with the assistance of a large language model [23] and the DT model maintained at the BS. The HL command is assumed to consist of N_{HL} packets, each of size n_{HL} bits each¹. At the BS, the HL command is converted into detailed control signals, referred to as low-level (LL) commands, which are transmitted from the BS to the RA. The LL commands consist of N_{LL} packets, each containing n_{LL} bits.

PF data is typically small in size and represents numeric values, such as the speed of the RA and the temperature of

¹Typically, there is one packet containing the specific command signals. However, the analysis in this paper does not specify the value of the number of packets for both HL and low-level, as the proposed framework and analysis are general.

the remote environment [7]. The PF data is collected at fixed, short intervals every T_s seconds and can be displayed on UE without further processing. However, the PF data is queued at both the RA and the BS. We denote n_{PF} (in bits) as the size of a PF packet.

Finally, ET data is generated by the RA in response to an LL command. ET data is generally throughput-intensive and may include multimedia data such as video, tactile details, and audio. Thus, the RA first compresses the ET data before transmitting it to the BS. The MEC server at BS decompresses the data, extracts valuable information (VI) from the ET data, such as the location and texture of the objective, and updates its DT model in preparation for the next loop. After processing, the VI is encoded into N_{VI} packets, each with an equal size of n_{VI} bits. The VI is then transmitted to the UE. The total size of the original ET data at the RA is denoted as n_{ET} (in bits). The compressed data (CD) is transmitted using N_{CD} packets, each containing n_{CD} bits.

The focus of this paper is on the closed-loop latency, T , of a single transmission round under various constraints on the individual links. Specifically, a single transmission round begins with the transmission of an HL command by the UE and lasts until the UE has received both the corresponding ET data *and* the PF data generated closest to the time instant when the LL data is received by the RA. The proposed framework in the following subsections incorporates the latency requirements for CL and the jitter between two heterogeneous information flows in FL. These requirements will affect T by influencing the latency of CL and FL. In scenarios involving multiple transmissions, additional queuing delay is introduced. We leave the analysis of the scenario with multiple transmissions for future work.

B. Latency Components

Based on the previous description and Fig. 2, the transmission latency of the PF data, denoted by T_{PF} , is given by

$$T_{PF} = T_{PF1}^q + T_{PF1}^{cm} + T_{PF2}^q + T_{PF2}^{cm}, \quad (1)$$

where T_{PF1}^q and T_{PF1}^{cm} denote the queuing and transmission delays from the RA to the BS, respectively, and T_{PF2}^q and T_{PF2}^{cm} denote the queuing and transmission delays from the BS to the UE, respectively. For the control data, the latency from UE to RA can be written

$$T_{CL} = T_{HL}^{cm} + T_{LL}^{cp} + T_{LL}^{cm}, \quad (2)$$

where T_{HL}^{cm} and T_{LL}^{cm} denote the transmission delay of the HL command and the LL command, respectively, and T_{LL}^{cp} denotes the processing delay at the BS. Similarly, the latency of transmitting ET data from the RA to the UE is

$$T_{ET} = T_{ET}^c + T_{CD}^{cm} + T_{ET}^d + T_{VI}^{cp} + T_{VI}^{cm}, \quad (3)$$

where T_{ET}^c denotes the compression delay at the RA, T_{CD}^{cm} and T_{VI}^{cm} denote the transmission delay from the RA to the BS and from the BS to the UE, respectively, and T_{ET}^d and T_{VI}^{cp} denote the decompression delay and the processing delay at the BS, respectively.

Recall that we are interested in the closed-loop latency from the generation of the HL command until the reception of both the corresponding ET data and the PT data generated closest in time to the generation time of the ET data. Given that the interval of the periodic transmission, T_s , is relatively small, its impact is negligible, and the latency of the feedback link, denoted as T_{FL} , can thus be approximated by

$$T_{FL} \approx \max \{T_{PF}, T_{ET}\}. \quad (4)$$

Using this, we finally write the closed-loop latency as

$$T = T_{CL} + T_{FL}. \quad (5)$$

Finally, we also define the jitter of the feedback link as the absolute difference between T_{ET} and T_{PF} , i.e., $|T_{ET} - T_{PF}|$.

C. Wireless Channel

We assume independent block fading channels at all links and the channel gain remains constant over the length of a transmitting packet. Assuming a transmission power of P_i , at link $i \in \{\text{HL}, \text{LL}, \text{PF1}, \text{PF2}, \text{CD}, \text{VI}\}$, the signal-to-noise ratio (SNR) at the receiver is given by

$$\text{SNR}_i = \frac{d_i^{-\ell_i} |h_i|^2 P_i}{N_0 B_i}, \quad i \in \{\text{HL}, \text{LL}, \text{PF1}, \text{PF2}, \text{CD}, \text{VI}\}, \quad (6)$$

where $|h_i|^2$ is the small-scale channel power gain, d_i is the distance between the transmitter and the receiver, ℓ_i is the path-loss exponent, N_0 is the spectral density of the noise power, and B_i is the bandwidth. For $i \in \{\text{LL}, \text{CD}, \text{PF1}\}$, d_i refers to the distance between the RA and BS, which we denote as d_{RB} . For $i \in \{\text{HL}, \text{PF2}, \text{VI}\}$, d_i refers to the distance between the BS and UE, which we denote as d_{BU} . Besides, we let ℓ_{BU} denote the path-loss exponent of the link between the BS and UE, while ℓ_{RB} denotes the path-loss exponent of the link between the RA and BS. Moreover, $B_{PF1} = B_{PF2} = B_{PF}$, while $B_{CD} = B_{VI} = B_{ET}$. In the case where channel state information is known only at the receiver side (CSIR), the transmitter adopts the ϵ_i -outage rate R_i . With $|h_i|^2 \sim \exp(1)$, the relationship between R_i and ϵ_i is given by [24]

$$R_i = B_i \log_2 \left(1 - \frac{d_i^{-\ell_i} P_i}{N_0 B_i} \ln(1 - \epsilon_i) \right). \quad (7)$$

For completeness, we also consider the case in which the transmitter also has perfect channel state information for the transmission of PF packets, referred to as CSIRT. In this case, we further assume that frequency or spatial diversity (FSD) is available, e.g., through multiple antennas. This is motivated by our previous work [25], [26], which demonstrates that with both CSIRT and FSD, the delay violation probability can be ensured to be zero with finite average power. In this case, we let τ_{PF} denote the deadline for PF data with CSIRT and FSD, indicating that the latency of each PF packet can not exceed τ_{PF} . Thus, with CSIRT and FSD, we can use τ_{PF} to represent

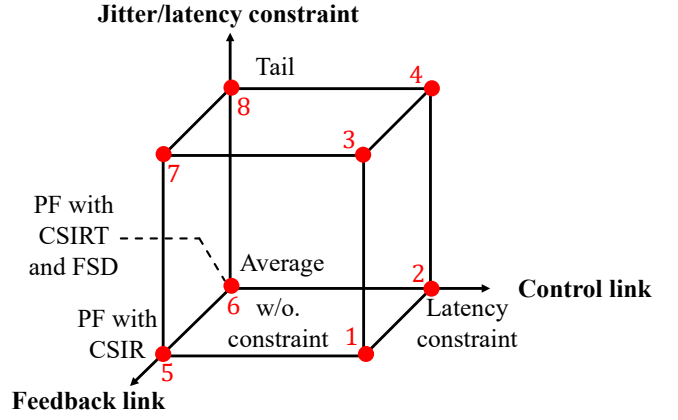


Fig. 3. Configurations considered in the proposed framework.

the latency of PF data.² Moreover, we let τ_{PF1} and τ_{PF2} denote the deadlines for the PF data transmission from the RA to BS and the BS to UE, respectively, satisfying $\tau_{PF1} + \tau_{PF2} \leq \tau_{PF}$.

D. A Unified Framework of Timing Constraints for CGC Systems with Different Configurations

In this subsection, we establish a unified timing-analysis framework for CGC systems under different configurations, shown as vertices in Fig. 3. The proposed framework ensures the timeliness performance of CL and the jitter performance of FL to cover general requirements for CGC systems. These constraints also influence the closed-loop latency T through T_{CL} and T_{FL} to ensure the reliability of CGC systems.

As depicted on the jitter/latency constraint axis, we consider both average and tail-based constraints on jitter and latency. Average-based constraints are related to the expectation of timing metrics, while tail-based constraints are related to the violation probability of timing metrics. For the CL, which handles the transmission of control data, we account for both configurations with and without a latency constraint representing a timeliness requirement on T_{CL} . Additionally, the FL may or may not have CSIRT and FSD for the PF data, as represented by the last axis. When CSIRT and FSD are available, a hard delay constraint is imposed on the PF data, denoted by τ_{PF} , as discussed in Section II-C. Under this condition, the PF transmission latency T_{PF} is treated as deterministic, where $T_{PF} = \tau_{PF}$. When only CSIR is available, T_{PF} becomes a random variable.

Regarding delay jitter, two different evaluation methods correspond to the different configurations along the FL axis in Fig. 3. The first method applies when the transmission of PF data benefits from both CSIRT and FSD. In this case, the latency of PF data is determined by the threshold τ_{PF} . Consequently, the jitter is defined as $|T_{ET} - \tau_{PF}|$.

The second method applies when the transmission of PF data only has CSIR, resulting in the stochastic latency of

²Although the average power is finite, the required instantaneous power may be large. If there is a maximum power constraint, the delay violation probability of the packet is not zero and can be characterized by large deviation theory [25] and extreme value theory [15]. The analysis of this setting is left for future work.

transmitting PF data. In this case, jitter is the difference between two random variables, expressed as $|T_{ET} - T_{PF}|$.

Based on these constraints along each axis, we can combine them to generate the eight vertices of the cube illustrated in Fig. 3.³ In the following, we elaborate on each vertex in Fig. 3. Vertices 1-4 refer to interactive systems where RA is controlled under different configurations as shown in Fig. 1.

- Vertex 1 – average constraints for CL and PF with CSIR:

$$\begin{cases} \mathbb{E}\{T_{CL}\} \leq \varrho_{CL}, \\ \mathbb{E}\{|T_{ET} - T_{PF}|\} \leq \varrho_{FLd}, \end{cases} \quad (8)$$

where ϱ_{CL} represents the average latency constraint of CL, and ϱ_{FLd} denotes the average jitter constraint of FL.

- Vertex 2 – average constraints for CL and PF with CSIRT and FSD:

$$\begin{cases} \mathbb{E}\{T_{CL}\} \leq \varrho_{CL}, \\ \tau_{PF1} + \tau_{PF2} \leq \tau_{PF}, \\ \mathbb{E}\{(T_{ET} - \tau_{PF})^+\} \leq \varrho_{FLs}, \end{cases} \quad (9)$$

where τ_{PF} and ϱ_{FLs} are average jitter constraints of FL. In this case, we treat the part in which $T_{ET} < \tau_{PF}$ as no jitter. This is because τ_{PF} is deterministic so that both ET and PF feedback can be shown to UE until PF data is received if $T_{ET} < \tau_{PF}$. Note that the third constraint in this case can be rewritten as

$$\mathbb{E}\{T_{ET} - \tau_{PF} | T_{ET} > \tau_{PF}\} \leq \frac{\varrho_{FLs}}{\Pr\{T_{ET} > \tau_{PF}\}}, \quad (10)$$

which can be seen as a condition value-at-risk (CVaR) based constraint [27].

- Vertex 3 – tail constraints for CL and PF with CSIR:

$$\begin{cases} \Pr\{T_{CL} < \tau_{CL}\} \geq \eta_{CL}, \\ \Pr\{|T_{ET} - T_{PF}| < \tau_{td}\} \geq \eta_{td}, \\ \text{Var}\{|T_{ET} - T_{PF}|\} \leq \rho_{td}, \end{cases} \quad (11)$$

where η_{CL} and τ_{CL} represent the tail latency constraints of CL. The parameters τ_{td} , η_{td} , and ρ_{td} denote the tail jitter constraints of FL. For the first constraint in Eq. (11), if η_{CL} is specified, the minimum τ_{CL} becomes the value at risk (VaR) [27], i.e.,

$$\tau_{CL} = \inf_t \{\Pr\{T_{CL} < t\} \geq \eta_{CL}\}. \quad (12)$$

If τ_{CL} is given, solving the maximum value of η_{CL} is equal to minimizing the delay violation probability, i.e.,

$$\eta_{CL} = \inf_p \{\Pr\{T_{CL} \geq \tau_{CL}\} \leq p\}. \quad (13)$$

The second and third constraints in Eq. (11) refer to the tail jitter constraint for FL. In addition to the violation probability of $|T_{ET} - T_{PF}|$, the variance of the jitter is included to cover general cases, serving as an important measurement for tail behavior, as demonstrated in [28].

³Note that except the constraints at the vertices of the cube, intermediate constraints can also be formed, such as a combination of tail-based FL constraints with average-based CL constraints. These constraints can be visualized as points between vertices i and $i + 2$, where $i \in \{1, 2, 5, 6\}$. Due to space limits, we omit detailed discussions.

- Vertex 4 – tail constraints for CL and PF with CSIRT and FSD:

$$\begin{cases} \Pr\{T_{CL} < \tau_{CL}\} \geq \eta_{CL}, \\ \tau_{PF1} + \tau_{PF2} \leq \tau_{PF}, \\ \Pr\{T_{ET} < \tau_{PF}\} \geq \eta_{ts}, \\ \text{Var}\{T_{ET} - \tau_{PF}\} \leq \rho_{ts}, \end{cases} \quad (14)$$

where τ_{PF} , η_{ts} and ρ_{ts} represent the tail jitter constraints of FL. Since τ_{PF} is a constant, the fourth constraint in Eq. (14) is equivalent to

$$\text{Var}\{T_{ET}\} \leq \rho_{ts}. \quad (15)$$

- Vertices 5-8 correspond to vertices 1-4 but omit the first constraint in Eqs. (8), (9), (11), and (14), respectively. In these vertices, there are no specific constraints for the CL. The focus is primarily on the performance of the closed-loop latency and FL's jitter, which applies to systems without the control for RA, such as the authorization of avatar usage rights mentioned in Section I-A.

It is important to obtain the distributions of T_{PF1}^q and T_{PF2}^q for modeling vertices 1, 3, 5, and 7. However, to the best of the authors' knowledge, no conclusive results exist for these distributions.⁴ Thus, we focus on the modeling and analysis of vertices 2, 4, 6, and 8 in the following parts, which correspond to cases where the transmission of PF data has CSIRT and FSD. Given the distribution of the inter-arrival time, the proposed framework and analyzing method can also be extended to other goal-oriented metrics, such as the age of information [29], age of loop [19], [14], and age of incorrect information [30]. Moreover, large deviation theory can be applied to model the queueing processes at the BS and RA for ET data [31], [32], capturing the asymptotic distribution of queueing latency. These extensions are left for future work.

III. STOCHASTIC LATENCY COMPONENTS AND A UNIFIED OPTIMIZATION PROBLEM IN CGC SYSTEMS

In this section, we will analyze the distribution of communication, computation, compression, and decompression latency in CGC systems. A unified optimization problem is formulated by integrating various constraints and stochastic latency components.

A. Distributions of Latency Components in CGC Systems

We start with the introduction of the communication latency. The latency for transmitting a packet, denoted as t_i where $i \in \{\text{HL}, \text{LL}, \text{PF1}, \text{PF2}, \text{CD}, \text{VI}\}$, satisfies $t_i = \frac{n_i}{R_i}$. Thus, the total time to successfully transmit a packet follows a geometric distribution. As defined in Section II-A, T_i^{cm} denotes the transmission latency for N_i packets, which follows a negative binomial distribution $\text{NB}(N_i, 1 - \epsilon_i)$. The PDF of T_i^{cm} is given by

$$\Pr\{T_i^{\text{cm}} = (N_i + k)t_i\} = \binom{k + N_i - 1}{N_i - 1} (1 - \epsilon_i)^{N_i} \epsilon_i^k, \quad (16)$$

⁴Once these distributions are known, vertices 1, 3, 5, and 7 can be analytically modeled using the proposed method in this paper.

where $k \in \{0, 1, \dots\}$.

PF data is collected every T_s seconds. Thus, a packet containing the PF data arrives at the buffer every T_s seconds, which leads to queuing delays. For vertices 2, 4, 6, and 8, we consider the case where CSIRT and FSD are available for the transmission of PF data. With CSIRT and FSD, the deadline constraint can be satisfied using finite average power [25]. Specifically, for $j \in \{\text{PF1}, \text{PF2}\}$, the deadline-constrained capacity is approximated by [26], [33]

$$R_j = B_j \log_2 \left(1 + \frac{c_1 d_j^{-\ell_j} P_j}{N_0 B_j (c_2 + (\tau_j)^{-c_3})} \right), \quad (17)$$

where $c_i > 0$, $i \in \{1, 2, 3\}$ are constants. For BS-to-UE transmission, the arrival of PF data is not periodic, but it can be regularized by reintegration, i.e., allowing one packet into the transmitting buffer even if multiple packets arrive in the same time slot. Therefore, the conclusion is valid. According to our previous conclusions in [26] and [33], by transmitting the PF data through two antennas with maximum-ratio combining, the closed-form approximation for the deadline-constrained capacity is

$$R_j = B_j \log_2 \left(1 + \frac{2.8771 d_j^{-\ell_j} P_j}{N_0 B_j (1.8771 + (\tau_j)^{-3.411})} \right). \quad (18)$$

By this means, to ensure that all PF data is transmitted within τ_j , the average power P_j can be determined from Eq. (18) by setting $R_j = \frac{n_{\text{PF}}}{T_s}$.

Next, we introduce the formulation of the computation time. As shown in Fig. 2, there are two feature extraction procedures in the CGC system, which are computed at the MEC server. For $l \in \{\text{LL}, \text{VI}\}$, the computation time is given by

$$T_l^{\text{CP}} = \frac{\tilde{n}_l X_l^{\text{CP}}}{\chi_{\text{MEC}}}, \quad (19)$$

where χ_{MEC} is the frequency of the processing unit at the MEC server, and X_l^{CP} is the number of processing-unit cycles required for processing 1-bit data. Here, $\tilde{n}_{\text{LL}} = N_{\text{HL}} n_{\text{HL}}$ and $\tilde{n}_{\text{VI}} = n_{\text{ET}}$. According to prior research [8]–[10], the number of cycles allocated to compute 1 bit is stochastic in nature. For the CPU case, X_l^{CP} follows a gamma distribution $\text{Gamma}(\alpha_{\text{MEC}}, \beta_l)$ [8]–[10], where α_{MEC} and β_l are the shape and rate parameters of the gamma distribution, respectively. The shape parameter remains the same for all tasks performed by the same processor, while the scale parameter β_l will be different for different tasks [8]. Consequently, the computation time follows a gamma distribution $\text{Gamma}\left(\alpha_{\text{MEC}}, \frac{\chi_{\text{MEC}} \beta_l}{\tilde{n}_l}\right)$. The PDF of T_l^{CP} is given by

$$f_l^{\text{CP}}(x) = \frac{(\chi_{\text{MEC}} \beta_l)^{\alpha_{\text{MEC}}}}{\tilde{n}_l^{\alpha_{\text{MEC}}} \Gamma(\alpha_{\text{MEC}})} x^{\alpha_{\text{MEC}}-1} \exp\left(-\frac{\chi_{\text{MEC}} \beta_l}{\tilde{n}_l} x\right), \quad (20)$$

where $x > 0$. The expectation of T_l^{CP} is $\mu_l^{\text{CP}} = \frac{\tilde{n}_l \alpha_{\text{MEC}}}{\chi_{\text{MEC}} \beta_l}$, while its variance is $\xi_l^{\text{CP}} = \frac{\tilde{n}_l^2 \alpha_{\text{MEC}}}{(\chi_{\text{MEC}} \beta_l)^2} \cdot 5$.

For the compression time, we define $\kappa \in [1, \kappa_{\text{max}}]$ as

the compression ratio, which is the ratio of the size of raw data to that of compressed data. Here, κ_{max} denotes the maximum compression ratio. Let X_c denote the number of CPU cycles required for compressing 1-bit data, which follows $\text{Gamma}(\alpha_{\text{RA}}, \beta_c)$, where α_{RA} and β_c denote the shape and rate parameters of compression latency, respectively. Let $\zeta_c(\kappa) = \mathbb{E}\{X_c\}$, which is an increasing function of κ . There are two primary conclusions in the literature for evaluating the expected computation load given a specific compression ratio. However, it remains unclear which conclusion is more applicable and what the exact range of application for each is. Therefore, we consider both conclusions to enhance the comprehensiveness of our analysis. We use $X_c^{(1)}$ and $X_c^{(2)}$ to distinguish between these two different conclusions. The first conclusion shows that

$$\mathbb{E}\{X_c^{(1)}\} = \frac{\alpha_{\text{RA}}}{\beta_c} = \exp(\psi\kappa) - \exp(\psi), \quad (21)$$

where $\psi > 0$ is a constant. This model can be used for several lossless compression techniques such as Zlib, Zstandard, and XZ compression [8], [9], [34]. Another conclusion shows that

$$\mathbb{E}\{X_c^{(2)}\} = \frac{\alpha_{\text{RA}}}{\beta_c} = \omega_1 (\omega_2 \kappa^{\omega_3} + \omega_4), \quad (22)$$

where ω_k , $k = 1, \dots, 4$ are positive constants for lossless compression algorithms GZIP and BZ2 as shown in [35].⁶ According to [35], Eq. (22) is also applicable to Zlib and XZ compression. Most of our analyses do not depend on the form of $\zeta_c(\kappa)$. For some discussions in Sections IV-C, IV-D, and V, we will specify which form we consider for $\zeta_c(\kappa)$.

Let X_d denote the number of CPU cycles for decompressing 1-bit data. X_d follows $\text{Gamma}(\alpha_{\text{MEC}}, \beta_d)$, where β_d is the rate parameter of decompression latency. Let $\zeta_d(\kappa) = \mathbb{E}\{X_d\}$. Accordingly, there are two primary conclusions in the literature for evaluating $\mathbb{E}\{X_d\}$. We use $X_d^{(1)}$ and $X_d^{(2)}$ to differentiate between the two different conclusions in existing works, corresponding to $X_c^{(1)}$ and $X_c^{(2)}$, respectively. The first conclusion shows that

$$\mathbb{E}\{X_d^{(1)}\} = \frac{\alpha_{\text{MEC}}}{\beta_d} = \omega_0 (\exp(\psi\kappa) - \exp(\psi)), \quad (23)$$

where $\omega_0 \in (0, 1)$ is a constant. Another conclusion shows

$$\mathbb{E}\{X_d^{(2)}\} = \frac{\alpha_{\text{MEC}}}{\beta_d} = \omega_5 (\omega_6 \kappa^{\omega_7} + \omega_8), \quad (24)$$

where ω_5 , ω_6 , and ω_8 are positive constants. The sign of ω_7 is determined by the specific compression algorithms [35].

With the above models and definitions, $T_{\text{ET}}^{\text{c}} = \frac{n_{\text{ET}} X_c}{\chi_{\text{RA}}}$, and $T_{\text{ET}}^{\text{d}} = \frac{n_{\text{ET}} X_d}{\kappa \chi_{\text{MEC}}}$, where χ_{RA} is the frequency of the processing unit at RA. Thus, we obtain $T_{\text{ET}}^{\text{c}} \sim \text{Gamma}\left(\alpha_{\text{RA}}, \frac{\chi_{\text{RA}} \alpha_{\text{RA}}}{n_{\text{ET}} \zeta_c(\kappa)}\right)$, with expectation $\mu_{\text{ET}}^{\text{c}} = \frac{n_{\text{ET}} \zeta_c(\kappa)}{\chi_{\text{RA}}}$ and variance $\xi_{\text{ET}}^{\text{c}} = \frac{(n_{\text{ET}} \zeta_c(\kappa))^2}{\chi_{\text{RA}}^2 \alpha_{\text{RA}}}$. $T_{\text{ET}}^{\text{d}} \sim \text{Gamma}\left(\alpha_{\text{MEC}}, \frac{\chi_{\text{MEC}} \alpha_{\text{MEC}} \kappa}{n_{\text{ET}} \zeta_d(\kappa)}\right)$, with expectation $\mu_{\text{ET}}^{\text{d}} = \frac{n_{\text{ET}} \zeta_d(\kappa)}{\chi_{\text{MEC}} \kappa}$ and variance $\xi_{\text{ET}}^{\text{d}} = \frac{(n_{\text{ET}} \zeta_d(\kappa))^2}{(\chi_{\text{MEC}} \kappa)^2 \alpha_{\text{MEC}}}$.

⁵Note that the analysis in this paper is also valid for GPU scenarios if the distribution of X_l^{CP} for GPU is given.

⁶Note that this model can also be used for evaluating $\mathbb{E}\{X_c\}$ of the lossy compression [35], e.g., JPEG.

B. Formulation of a Unified Optimization Problem

In this subsection, we will formulate a unified optimization problem for this CGC system, in which average-based and tail-based optimization objectives and constraints are considered.

The optimization objective can be framed from various aspects. If our goal is to reduce the closed-loop latency to enhance reliability and provide a better experience for users, the objective function is related to the closed-loop latency T . If we aim to save resources, e.g., power and bandwidth, the objective function is related to the average power and bandwidth.

For the first kind of objective functions, we also consider two cases, i.e., the average-based and tail-based objectives. The average-based objective is associated to $\mathbb{E}\{T\}$. For the tail-based objective, let T_{th} denote the threshold for the closed-loop latency, which is determined by the specific applications and user's requirements. Thus, the tail-based objective is related to $\Pr\{T < T_{\text{th}}\}$. We define $d(T)$ as the objective function associated with T . Besides, we define $g(P_{\text{avg}}, B)$ as the objective function related to resources. We also assume that $d(T)$ and $g(P_{\text{avg}}, B)$ are normalized.

A unified optimization problem for this CGC system is then formulated by combining different kinds of objectives and constraints.

$$\min \quad \varepsilon d(T) + (1 - \varepsilon)g(P_{\text{avg}}, B) \quad (25a)$$

$$\text{s.t.} \quad \text{Constraints of a vertex in Fig. 3,} \quad (25b)$$

$$P_{\text{PF1}} + P_{\text{CD}} \leq P_{\text{RA}}^{\text{th}}, \quad (25c)$$

$$P_{\text{PF2}} + P_{\text{VI}} \leq P_{\text{BS}}^{\text{th}}, \quad (25d)$$

$$B_{\text{PF}} + B_{\text{ET}} = B, \quad (25e)$$

where $\varepsilon \in [0, 1]$, $P_{\text{RA}}^{\text{th}}$ and $P_{\text{BS}}^{\text{th}}$ denote the average power constraints for the RA and BS, respectively. We set $B_{\text{PF1}} = B_{\text{PF2}} = B_{\text{PF}}$, and B (in Hz) represents the maximum available bandwidth. Eq. (25b) allows us to select a vertex based on scenario requirements, with each vertex corresponding to the specific constraints outlined in Section II-D. For $\varepsilon = 0$, we are interested in designing a resource-efficient scheduling. For $\varepsilon = 1$, the focus is on optimizing the performance of closed-loop latency. The optimization variables in this problem may include $\{\kappa, B_{\text{PF}}, B_{\text{ET}}, P_{\text{PF1}}, P_{\text{PF2}}, \tau_{\text{PF1}}, \tau_{\text{PF2}}, P_{\text{CD}}, P_{\text{VI}}\}$.

It is not trivial work to solve this optimization problem in CGC systems. As demonstrated in Section III-A, the expectation and variance of each latency component in this system are known, which can be used to characterize some constraints related to the expectation and variance of T_{ET} . However, regardless of the vertex constraints chosen, we have to obtain the distribution of closed-loop and FL's latency. For vertices 2 and 4, the CDF of CL latency is also required. Since the latency of CL, FL, and the closed loop are sums of gamma and negative binomial random variables, obtaining analytical distributions for these latency is challenging. Thus, it is crucial to derive the analytical expression for the distribution of CL, FL, and closed-loop latency in general scenarios for enabling efficient performance evaluation or optimization.

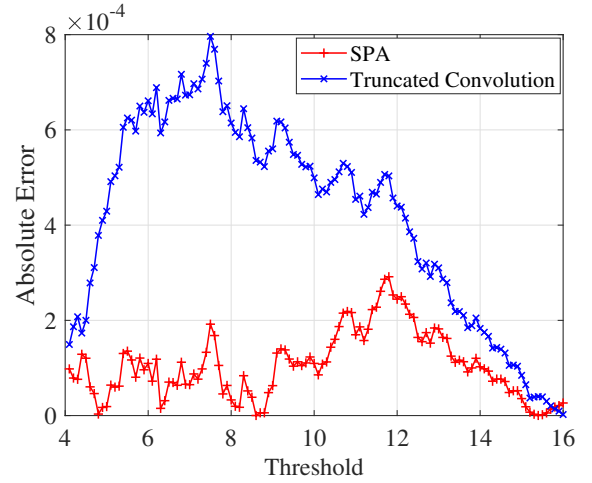


Fig. 4. Comparison between the SPA and the truncated convolution used in [8].

IV. ANALYTICAL EXPRESSION OF THE LATENCY DISTRIBUTION IN CGC SYSTEMS

In this section, we will present a general method for approximating the distribution of CL, FL, and closed-loop latency. Based on this general method, we also provide methods for efficiently evaluating the terms in various constraints. Since there are similarities in the latency distributions and constraints of CL, FL, and closed-loop latency, we will take FL for example to show how to derive the analytical expression for the terms in the proposed constraints for FL. We will then present the results of CL and closed-loop latency without detailed proofs. For simplicity, we define $T_1 = T_{\text{CL}} + T_{\text{ET}}$. Without loss of generality, we let $t_{\text{CD}} = t_{\text{VI}} = t_{\text{u}}$.

A. A General Method for Analytical Approximation for the CDF of Latency

From Section III, we find that there are both discrete and continuous random variables among the components of CL, FL, and closed-loop latency. We have to treat them separately due to their different properties. We will first present a general method to approximate the CDF of T_{ET} , which can be applied to the CDF approximations of T_{CL} , T_{FL} , and T .

In Lemma 1, we derive the analytical expression for the CDF of $T_{\text{ET}}^c + T_{\text{ET}}^d + T_{\text{VI}}^{\text{cp}}$ with the help of SPA. For simplicity, let $F_1(x)$ and $f_1(x)$ denote the CDF and PDF, respectively, of $T_{\text{ET}}^c + T_{\text{ET}}^d + T_{\text{VI}}^{\text{cp}}$, which is a sum of continuous random variables. Besides, we let

$$\iota_1 = \left(\frac{n_{\text{ET}}^2 \zeta_c^2(\kappa)}{\chi_{\text{RA}}^2 \alpha_{\text{RA}}} + \frac{n_{\text{ET}}^2 \zeta_d^2(\kappa)}{\chi_{\text{MEC}}^2 \kappa^2 \alpha_{\text{MEC}}} + \frac{n_{\text{ET}}^2 \alpha_{\text{MEC}}}{\chi_{\text{MEC}}^2 \beta_{\text{VI}}^2} \right)^{\frac{3}{2}}, \quad (26)$$

$$\iota_2 = \frac{2n_{\text{ET}}^3 \zeta_c^3(\kappa)}{\chi_{\text{RA}}^3 \alpha_{\text{RA}}^2} + \frac{2n_{\text{ET}}^3 \zeta_d^3(\kappa)}{\kappa^3 \chi_{\text{MEC}}^3 \alpha_{\text{MEC}}^2} + \frac{2\alpha_{\text{MEC}} n_{\text{ET}}^3}{\chi_{\text{MEC}}^3 \beta_{\text{VI}}^3}, \text{ and} \quad (27)$$

$$\theta = \frac{n_{\text{ET}} \alpha_{\text{MEC}}}{\chi_{\text{MEC}} \beta_{\text{VI}}} + \frac{n_{\text{ET}} \zeta_c(\kappa)}{\chi_{\text{RA}}} + \frac{n_{\text{ET}} \zeta_d(\kappa)}{\chi_{\text{MEC}} \kappa}. \quad (28)$$

Lemma 1. With θ defined in Eq. (28),

- the CDF of $T_{\text{ET}}^{\text{c}} + T_{\text{ET}}^{\text{d}} + T_{\text{VI}}^{\text{cp}}$ is approximated by

$$F_1(x) \approx \begin{cases} \Phi(v_x) + \phi(v_x) \left(\frac{1}{v_x} - \frac{1}{u_x} \right), & x \neq \theta, \\ \frac{1}{2} + \frac{\nu_2}{6\sqrt{2\pi}\iota_1}, & x = \theta, \end{cases} \quad (29)$$

where

$$\begin{aligned} v_x &= \text{sign}(\Xi_1(x)) \sqrt{2x\Xi_1(x) - 2L(\Xi_1(x))}, \text{ and} \\ u_x &= \Xi_1(x) \sqrt{L''(\Xi_1(x))}. \end{aligned} \quad (30)$$

$\Xi_1(\cdot)$ is the inverse function of $L'(\cdot)$. ι_1 and ι_2 are given in Eqs. (26) and (27), respectively. $L(\cdot)$ is given in Eq. (31), where $s < \min \left\{ \frac{\chi_{\text{RA}}\alpha_{\text{RA}}}{n_{\text{ET}}\zeta_{\text{c}}(\kappa)}, \frac{\chi_{\text{MEC}}\alpha_{\text{MEC}}\kappa}{n_{\text{ET}}\zeta_{\text{d}}(\kappa)}, \frac{\chi_{\text{MEC}}\beta_{\text{VI}}}{n_{\text{ET}}} \right\}$.

- the PDF of $T_{\text{ET}}^{\text{c}} + T_{\text{ET}}^{\text{d}} + T_{\text{VI}}^{\text{cp}}$ is approximated by

$$f_1(x) \approx \frac{\exp(L(\Xi_1(x)) - x\Xi_1(x))}{\sqrt{2\pi L''(\Xi_1(x))}}, \quad x > 0. \quad (32)$$

Proof: See Appendix A. \blacksquare

In Lemma 1, we derive the CDF and PDF of $T_{\text{ET}}^{\text{c}} + T_{\text{ET}}^{\text{d}} + T_{\text{VI}}^{\text{cp}}$, which is the sum of continuous components of T_{ET} . For T_1 , the sum of continuous components is $T_{\text{LL}}^{\text{cp}} + T_{\text{ET}}^{\text{c}} + T_{\text{ET}}^{\text{d}} + T_{\text{VI}}^{\text{cp}}$. Thus, we define $\tilde{L}(s)$ as

$$\tilde{L}(s) = L(s) - \alpha_{\text{MEC}} \ln \left(1 - \frac{N_{\text{HL}}n_{\text{HL}}s}{\chi_{\text{MEC}}\beta_{\text{LL}}} \right), \quad (33)$$

where $s < \min \left\{ \frac{\chi_{\text{MEC}}\beta_{\text{LL}}}{N_{\text{HL}}n_{\text{HL}}}, \frac{\chi_{\text{RA}}\alpha_{\text{RA}}}{n_{\text{ET}}\zeta_{\text{c}}(\kappa)}, \frac{\chi_{\text{MEC}}\alpha_{\text{MEC}}\kappa}{n_{\text{ET}}\zeta_{\text{d}}(\kappa)}, \frac{\chi_{\text{MEC}}\beta_{\text{VI}}}{n_{\text{ET}}} \right\}$.

Besides, we let $\tilde{\iota}_1 = \left(\iota_1^{\frac{2}{3}} + \frac{N_{\text{HL}}^2 n_{\text{HL}}^2 \alpha_{\text{MEC}}}{\chi_{\text{MEC}}^2 \beta_{\text{LL}}^2} \right)^{\frac{3}{2}}$, $\tilde{\iota}_2 = \iota_2 + \frac{2\alpha_{\text{MEC}} N_{\text{HL}}^3 n_{\text{HL}}^3}{\chi_{\text{MEC}}^3 \beta_{\text{LL}}^3}$, and $\tilde{\theta} = \theta + \frac{N_{\text{HL}}n_{\text{HL}}\alpha_{\text{MEC}}}{\chi_{\text{MEC}}\beta_{\text{LL}}}$. By replacing $\tilde{L}(s)$, $\tilde{\iota}_1$, $\tilde{\iota}_2$, and $\tilde{\theta}$ into Eqs. (29) and (32), we obtain the CDF and PDF of $T_{\text{LL}}^{\text{cp}} + T_{\text{ET}}^{\text{c}} + T_{\text{ET}}^{\text{d}} + T_{\text{VI}}^{\text{cp}}$. We let $\tilde{F}_1(x)$ denote the CDF of $T_{\text{LL}}^{\text{cp}} + T_{\text{ET}}^{\text{c}} + T_{\text{ET}}^{\text{d}} + T_{\text{VI}}^{\text{cp}}$.

To show the advantages of SPA, we provide a comparison between SPA and the truncated convolution used in [8]. The comparison result is shown in Fig. 4. We consider the sum of $M = 4$ independent gamma random variables, each following $\text{Gamma}(2, 1)$. The granularity of the truncated convolution is set to $\delta_1 = 10^{-3}$, and the truncated threshold is defined as $\Lambda_1 = 20$. The solution to the SPA equation is obtained through binary search with termination threshold $\delta_2 = 10^{-3}$ and an interval $[\Lambda_2, \Lambda_3]$, where $\Lambda_2 = -10^5$ and $\Lambda_3 = 1$. For SPA, the granularity is set to $\delta_3 = 10^{-3}$, and the truncated threshold is $\Lambda_4 = 16$. From Fig. 4, we observe that SPA achieves a smaller error than the truncated convolution in most cases. The complexity of the truncated convolution is $O\left(\left\lceil \frac{\Lambda_1}{\delta_1} \right\rceil^M\right)$ for the general cases where random variables are independent but not necessarily identically distributed. In contrast, the complexity of SPA is $O\left(\left\lceil \frac{\Lambda_4}{\delta_3} \right\rceil \log_2 \left\lceil \frac{\Lambda_3 - \Lambda_2}{\delta_2} \right\rceil\right)$, which is not related to M . Thus, SPA offers improved approximation accuracy while reducing the complexity for larger M .

Remark 1: The existing work has discussed the asymptotic

error of SPA for the CDF of the sum of i.i.d. random variables. For i.i.d. random variables Y_1, Y_2, \dots, Y_n , let $Y = \sum_{i=1}^n Y_i$, and let $\tilde{F}_Y(y)$ denote the SPA of its CDF, while $F_Y(y)$ denotes the true CDF of Y . The error of the SPA for CDF mainly results from the Laplace approximation [20, Eq. (2.5)] and Temme approximation [20, Eq. (2.34)]. According to [20, Eq. (2.46)], the relationship between $\tilde{F}_Y(y)$ and $F_Y(y)$ is given by

$$F_Y(y) = \tilde{F}_Y(y) + O(n^{-1}). \quad (34)$$

This error analysis can be viewed as a special case of the considered problem in this paper. For example, when T_{ET}^{c} , T_{ET}^{d} , $T_{\text{VI}}^{\text{cp}}$ are i.i.d. in Lemma 1, Eq. (34) holds. However, T_{ET}^{c} , T_{ET}^{d} , $T_{\text{VI}}^{\text{cp}}$ may not follow identical gamma distributions. For this case, we can also utilize the result of Eq. (2.46) in [20] to provide an intuitive analysis, though not rigorous. Assume that Y_i follows $\text{Gamma}(\alpha_i, \beta_i)$ and Y_i is independent of Y_j , $i \neq j$. For convenience of expression, we let $v_1 = \max_{i=1, \dots, n} \{\alpha_i\}$ and $v_2 = \min_{i=1, \dots, n} \{\beta_i\}$. Then, the CGF of $\sum_{i=1}^n Y_i$ can be expressed as

$$\begin{aligned} K_Y(s) &= - \sum_{i=1}^n \alpha_i \ln \left(1 - \frac{s}{\beta_i} \right) \\ &= n \underbrace{\left[-v_1 \ln \left(1 - \frac{s}{v_2} \right) \right] \left[\sum_{i=1}^n \frac{\alpha_i}{n v_1} \frac{\ln \left(1 - \frac{s}{\beta_i} \right)}{\ln \left(1 - \frac{s}{v_2} \right)} \right]}_{K_{\tilde{Y}}(s)}, \\ &= n \left[-v_1 \ln \left(1 - \frac{s}{v_2} \right) \right] (1 + O(n^{-1})), \quad s < v_2 \end{aligned} \quad (35)$$

Eq. (35) holds because $\frac{\alpha_i}{v_1} < 1$ and $\frac{\ln \left(1 - \frac{s}{\beta_i} \right)}{\ln \left(1 - \frac{s}{v_2} \right)}$ is bounded. The

boundness of $\frac{\ln \left(1 - \frac{s}{\beta_i} \right)}{\ln \left(1 - \frac{s}{v_2} \right)}$ can be shown by $\lim_{s \rightarrow v_2} \frac{\ln \left(1 - \frac{s}{\beta_i} \right)}{\ln \left(1 - \frac{s}{v_2} \right)} = 0$

with $\beta_i \neq v_2$, $\lim_{s \rightarrow v_2} \frac{\ln \left(1 - \frac{s}{\beta_i} \right)}{\ln \left(1 - \frac{s}{v_2} \right)} = 1$ with $\beta_i = v_2$, and

$$\lim_{s \rightarrow -\infty} \frac{\ln \left(1 - \frac{s}{\beta_i} \right)}{\ln \left(1 - \frac{s}{v_2} \right)} = \lim_{s \rightarrow -\infty} \frac{\ln \left(-\frac{s}{\beta_i} \right)}{\ln \left(-\frac{s}{v_2} \right)} = 1. \quad (36)$$

Eq. (35) indicates that we can treat $\sum_{i=1}^n Y_i$ as a summation of n i.i.d. random variables with CGF $K_{\tilde{Y}}(s)$ with error $O(n^{-1})$. The essence of this analysis is that the CGF of Y_i has a unified expression with different values of parameters. Combining Eqs. (35) and (34), we can approximately evaluate the error of SPA in Lemma 1. However, it is an important work to provide rigorous error analysis for SPA with non-i.i.d. random variables, which remains open and is beyond the scope of this paper. From Eq. (34), we find that SPA becomes more accurate with a larger n . However, as noted in [20] and demonstrated by the numerical results in Section V, SPA

$$L(s) = -\alpha_{\text{RA}} \ln \left(1 - \frac{n_{\text{ET}}\zeta_{\text{c}}(\kappa)s}{\chi_{\text{RA}}\alpha_{\text{RA}}} \right) - \alpha_{\text{MEC}} \ln \left(1 - \frac{n_{\text{ET}}\zeta_{\text{d}}(\kappa)s}{\chi_{\text{MEC}}\alpha_{\text{MEC}}\kappa} \right) - \alpha_{\text{MEC}} \ln \left(1 - \frac{n_{\text{ETS}}}{\chi_{\text{MEC}}\beta_{\text{VI}}} \right). \quad (31)$$

achieves satisfying accuracy with $n = 3$. To enhance accuracy, we can adopt the second-order SPA, which can be found in [20, Eq. (2.48)] with an error term $O(n^{-2})$. For the SPA of the PDF, the analysis is similar. We will elaborate on the error analysis for the SPA of the PDF in Remark 2, which is analogous to the error analysis for the PMF approximation.

In Lemma 2, we obtain the closed-form expression for the probability mass function (PMF) of $T_{\text{CD}}^{\text{cm}} + T_{\text{VI}}^{\text{cm}}$ with the help of saddlepoint mass functions. $T_{\text{CD}}^{\text{cm}} + T_{\text{VI}}^{\text{cm}}$ is a sum of discrete components of T_{ET} . For simplicity, let p_k denote $\Pr\{T_{\text{CD}}^{\text{cm}} + T_{\text{VI}}^{\text{cm}} = kt_{\text{u}}\}$, where $k \in \{N_{\text{CD}} + N_{\text{VI}}, N_{\text{CD}} + N_{\text{VI}} + 1, \dots\}$.

Lemma 2 The PMF of $T_{\text{CD}}^{\text{cm}} + T_{\text{VI}}^{\text{cm}}$ is approximated by

$$p_k \approx \begin{cases} (1 - \epsilon_{\text{CD}})^{N_{\text{CD}}}(1 - \epsilon_{\text{VI}})^{N_{\text{VI}}}, & k = N_{\text{CD}} + N_{\text{VI}}, \\ \frac{\exp(J(\Xi_2(k)) - k\Xi_2(k))}{\sqrt{2\pi \left(\frac{\epsilon_{\text{CD}} N_{\text{CD}} e^{\Xi_2(k)}}{(1 - \epsilon_{\text{CD}} e^{\Xi_2(k)})^2} + \frac{\epsilon_{\text{VI}} N_{\text{VI}} e^{\Xi_2(k)}}{(1 - \epsilon_{\text{VI}} e^{\Xi_2(k)})^2} \right)}}, & k > N_{\text{CD}} + N_{\text{VI}}, \end{cases} \quad (37)$$

where $\Xi_2(\cdot)$ is the inverse function of $J'(\cdot)$. $J(\cdot)$ is given in Eq. (38).

Proof: See Appendix B. ■

Remark 2: The existing work has conducted the error analysis for saddlepoint mass function with i.i.d. random variables Z_i , $i = 1, \dots, n$. Let $\{P_k\}$ denote the true PMF of $Z = \sum_{i=1}^n Z_i$, while $\{\tilde{P}_k\}$ denotes the saddlepoint mass function. Assuming that Z_i is i.i.d., we have [20, Eq. (2.24)]

$$P_k = \tilde{P}_k(1 + O(n^{-1})). \quad (39)$$

Eq. (39) can be used to analyze the approximation error in Lemma 2 when $T_{\text{CD}}^{\text{cm}}$ and $T_{\text{VI}}^{\text{cm}}$ are i.i.d.. When $T_{\text{CD}}^{\text{cm}}$ and $T_{\text{VI}}^{\text{cm}}$ are independent but not identically distributed, the analysis is similar to Remark 1. Assume that $Z_i \sim \text{NB}(N_i, 1 - \epsilon_i)$ and Z_i is independent of Z_j with $i \neq j$. The CGF of Z_i is denoted by $K_{Z_i}(s)$. Let $v_3 = \max\{N_i\}$, $v_4 = \max\{\epsilon_i\}$, and $v_5 = \min\{\epsilon_i\}$. Then, the CGF of Z can be written as Eq. (40). Eq. (40) indicates that we can treat Z as a summation of n i.i.d. random variables with CGF $K_{\tilde{Z}}(s)$. Thus, Eq. (39) can be used for the error analysis of Lemma 2. To achieve higher approximation accuracy, second-order SPA can be utilized, which is provided in [20, 2.32].

In Lemma 2, we derive the PMF of $T_{\text{CD}}^{\text{cm}} + T_{\text{VI}}^{\text{cm}}$, which is the sum of discrete components of T_{ET} . For T_1 , the sum of discrete components is $T_{\text{HL}}^{\text{cm}} + T_{\text{LL}}^{\text{cm}} + T_{\text{CD}}^{\text{cm}} + T_{\text{VI}}^{\text{cm}}$. We let \tilde{p}_k denote $\Pr\{T_{\text{HL}}^{\text{cm}} + T_{\text{LL}}^{\text{cm}} + T_{\text{CD}}^{\text{cm}} + T_{\text{VI}}^{\text{cm}} = kt_{\text{u}}\}$. Moreover, we let $\tilde{J}(s)$ denote the CGF of $T_{\text{HL}}^{\text{cm}} + T_{\text{LL}}^{\text{cm}} + T_{\text{CD}}^{\text{cm}} + T_{\text{VI}}^{\text{cm}}$.

Due to space limits, we omit the expression of $\tilde{J}(s)$, which is similar to Eq. (38). By substituting $\tilde{J}(s)$ into Eq. (37), we obtain \tilde{p}_k , where $k > N_{\text{HL}} + N_{\text{LL}} + N_{\text{CD}} + N_{\text{VI}}$. For $k = N_{\text{HL}} + N_{\text{LL}} + N_{\text{CD}} + N_{\text{VI}}$, we have

$$\tilde{p}_k = (1 - \epsilon_{\text{HL}})^{N_{\text{HL}}}(1 - \epsilon_{\text{LL}})^{N_{\text{LL}}} p_{N_{\text{CD}} + N_{\text{VI}}}. \quad (41)$$

Moreover, we also let p_k^{CL} denote the PMF of $T_{\text{HL}}^{\text{cm}} + T_{\text{LL}}^{\text{cm}}$, which is the sum of discrete component of T_{CL} . Due to space limits, we omit the derivation of p_k^{CL} , which is also similar to Eq. (37).

Based on Lemmas 1 and 2, CDFs of T_{CL} , T_{ET} , T_{FL} , T_1 and T can be derived for general scenarios. We let $F_{\text{CT}}(x)$, $F_{\text{ET}}(x)$, $F_{\text{FL}}(x)$, $F_{T_1}(x)$ and $F_T(x)$ denote the CDFs of T_{CL} , T_{ET} , T_{FL} , T_1 , and T , respectively.

Theorem 1. For vertices 2, 4, 6, and 8, the CDF of T_{CL} is given by

$$F_{\text{CL}}(x) \approx \sum_{k=N_{\text{HL}}+N_{\text{LL}}}^{\lfloor \frac{x}{t_{\text{u}}} \rfloor} \frac{p_k^{\text{CL}}}{\Gamma(\alpha_{\text{MEC}})} \gamma \left(\alpha_{\text{MEC}}, \frac{\chi_{\text{MEC}} \beta_{\text{LL}}(x - kt_{\text{u}})}{N_{\text{HL}} n_{\text{HL}}} \right), \quad (42)$$

where $x > 0$.

The CDF of T_{ET} is given by

$$F_{\text{ET}}(x) \approx \sum_{k=N_{\text{CD}}+N_{\text{VI}}}^{\lfloor \frac{x}{t_{\text{u}}} \rfloor} p_k F_1(x - kt_{\text{u}}), \quad x > 0. \quad (43)$$

The CDF of T_{FL} is given by

$$F_{\text{FL}}(x) \approx \mathbb{I}\{x > \tau_{\text{PF}}\} F_{\text{ET}}(x), \quad x > 0. \quad (44)$$

The CDF of T is given by

$$F_T(x) \approx \mathbb{I}\{x > \tau_{\text{PF}}\} F_{\text{CL}}(x - \tau_{\text{PF}}) F_{T_1}(x), \quad (45)$$

where $F_{T_1}(x)$ is given by

$$F_{T_1}(x) \approx \sum_{k=N_{\text{HL}}+N_{\text{LL}}+N_{\text{CD}}+N_{\text{VI}}}^{\lfloor \frac{x}{t_{\text{u}}} \rfloor} \tilde{p}_k \tilde{F}_1(x - kt_{\text{u}}), \quad x > 0. \quad (46)$$

Proof: The CDF of T_{CL} , T_{ET} , and T_1 can be obtained directly according to Lemmas 1 and 2. For T_{FL} , we can obtain its CDF based on $F_{\text{ET}}(x)$ and the definition of T_{FL} . For the closed-loop latency T , it can be expressed as $T = T_{\text{CL}} + T_{\text{FL}} = \max\{T_{\text{CL}} + \tau_{\text{PF}}, T_1\}$. Thus, the CDF of T is given by

$$\Pr\{T < x\} = \Pr\{T_{\text{CL}} < x - \tau_{\text{PF}}\} \Pr\{T_1 < x\}. \quad (47)$$

Then we obtain the CDF of T . ■

$$J(s) = N_{\text{CD}}(s + \ln(1 - \epsilon_{\text{CD}}) - \ln(1 - \epsilon_{\text{CD}} e^s)) + N_{\text{VI}}(s + \ln(1 - \epsilon_{\text{VI}}) - \ln(1 - \epsilon_{\text{VI}} e^s)), \quad s < \min\{-\ln \epsilon_{\text{CD}}, -\ln \epsilon_{\text{VI}}\}. \quad (38)$$

$$K_Z(s) = \underbrace{n v_3 (s + \ln(1 - v_5) - \ln(1 - v_4 e^s))}_{K_{\tilde{Z}}(s)} \left(\sum_{i=1}^n \frac{K_{Z_i}(s)}{n v_3 (s + \ln(1 - v_5) - \ln(1 - v_4 e^s))} \right) \quad (40)$$

$$= n v_3 (s + \ln(1 - v_5) - \ln(1 - v_4 e^s)) (1 + O(n^{-1})), \quad s < -\ln v_4.$$

Algorithm 1 Calculating CDF of T_{ET}

Input: parameter $\Delta \in (0, 1)$ for controlling the approximation accuracy

Output: $F_{\text{ET}}(x)$

```

1: Initialization:  $k = N_{\text{CD}} + N_{\text{VI}} - 1, \Theta = 0$ 
2: repeat
3:    $k \leftarrow k + 1$ 
4:   Calculate  $p_k$  according to Eq. (37)
5: until  $p_k < \Delta$ 
6:  $\nu \leftarrow \mathbb{I}\{k > N_{\text{CD}} + N_{\text{VI}}\} \sum_{i=N_{\text{CD}}+N_{\text{VI}}+1}^k p_i$ 
7: if  $\nu > 0$  then
8:   for all  $j = N_{\text{CD}} + N_{\text{VI}} + 1, \dots, k$  do
9:      $p_j \leftarrow (1 - p_{N_{\text{CD}}+N_{\text{VI}}}) \frac{p_j}{\nu}$ 
10:  end for
11: end if
12: if  $\lfloor \frac{x}{t_u} \rfloor < N_{\text{CD}} + N_{\text{VI}}$  then
13:    $\Theta \leftarrow 0$ 
14: else
15:   for all  $l = N_{\text{CD}} + N_{\text{VI}}, \dots, \min \left\{ \lfloor \frac{x}{t_u} \rfloor, k \right\}$  do
16:     Calculate  $F_1(x - lt_u)$  according to Eq. (29).
17:      $\Theta \leftarrow \Theta + p_l F_1(x - lt_u)$ 
18:   end for
19: end if
20:  $F_{\text{ET}}(x) \leftarrow \Theta$ 

```

In Theorem 1, we derive the CDFs for both CL, FL, and closed-loop latency. In practical applications, we can reduce the complexity of approximating $F_{\text{ET}}(x)$ by controlling the desired approximation accuracy. Based on Theorem 1, we conceive an algorithm for efficiently approximating $F_{\text{ET}}(x)$ in practical applications. The details of this algorithm are shown in Alg. 1. Steps 6 and 9 are used for normalizing the PMF of $T_{\text{CD}}^{\text{cm}} + T_{\text{VI}}^{\text{cm}}$. Similar procedures can be used to compute $F_{\text{CL}}(x)$ and $F_{\text{T}_1}(x)$.

B. Continuous Approximation for a Large Number of Packets or Small Transmission Time of a Packet

In the last subsection, we present a general method to approximate the latency distribution. Since the CL, FL, and closed-loop latencies consist of sums of continuous and discrete random variables, we adopt both the Lugannani-Rice (LR) formula [20, Eq. (1.21)] and saddlepoint mass function [20, Eq. (1.13)] to obtain a satisfying approximation performance. However, in practical applications, the number of packets is usually large. Besides, the transmission time of a packet can be small in short-packet scenarios. In this subsection, we focus on these cases, where either the number of packets is large or t_u is small. Under these conditions, we can apply the central limit theorem (CLT) to approximate the

sum of communication latency as normal random variables, thereby treating T_{FL} and T as continuous random variables.

We start with the analysis for the discrete components of T_{ET} , which can be generalized to the analysis for the discrete components of T . $T_{\text{CD}}^{\text{cm}}$ is the sum of N_{CD} i.i.d. discrete random variables, while $T_{\text{VI}}^{\text{cm}}$ is similar. Under the condition that $N_{\text{CD}} + N_{\text{VI}}$ is large, the discrete random variable $T_{\text{CD}}^{\text{cm}} + T_{\text{VI}}^{\text{cm}}$ can be approximated by a normal random variable, which is different from the general analysis in Lemma 2. That is, $T_{\text{CD}}^{\text{cm}} + T_{\text{VI}}^{\text{cm}} \sim \mathcal{N} \left(\frac{N_{\text{CD}} t_u}{1 - \epsilon_{\text{CD}}} + \frac{N_{\text{VI}} t_u}{1 - \epsilon_{\text{VI}}}, \frac{\epsilon_{\text{CD}} N_{\text{CD}} t_u^2}{(1 - \epsilon_{\text{CD}})^2} + \frac{\epsilon_{\text{VI}} N_{\text{VI}} t_u^2}{(1 - \epsilon_{\text{VI}})^2} \right)$. As analyzed in [8], we are interested in scenarios in which the negative value from Gaussian approximation has a negligible effect on the analysis. Moreover, $T_{\text{CD}}^{\text{cm}}$ and $T_{\text{VI}}^{\text{cm}}$ are both t_u -lattice random variables. Thus, we can treat $T_{\text{CD}}^{\text{cm}}$ and $T_{\text{VI}}^{\text{cm}}$ as continuous random variables when t_u is small. There are two possibilities for scenarios with small t_u from the perspective of the number of packets. The first possibility is that $N_{\text{CD}} + N_{\text{VI}}$ is small. Since t_u is also small, the corresponding transmission time has a small influence on the distribution of T . The second possibility is that the $N_{\text{CD}} + N_{\text{VI}}$ is large. Then we treat $T_{\text{CD}}^{\text{cm}} + T_{\text{VI}}^{\text{cm}}$ as a continuous random variable by CLT. In summary, we can use CLT to approximate the distribution of $T_{\text{CD}}^{\text{cm}} + T_{\text{VI}}^{\text{cm}}$ with large $N_{\text{CD}} + N_{\text{VI}}$ or small t_u .

Based on this continuous approximation, we can directly obtain the CDF and PDF approximation of T_{ET} according to the LR formula. We define the following constants as

$$\Psi = \theta + \vartheta t_u, \quad (48)$$

where

$$\vartheta = \frac{N_{\text{CD}}}{1 - \epsilon_{\text{CD}}} + \frac{N_{\text{VI}}}{1 - \epsilon_{\text{VI}}}. \quad (49)$$

We also define that

$$\Upsilon = \left(t_1^{\frac{2}{3}} + \frac{\epsilon_{\text{CD}} N_{\text{CD}} t_u^2}{(1 - \epsilon_{\text{CD}})^2} + \frac{\epsilon_{\text{VI}} N_{\text{VI}} t_u^2}{(1 - \epsilon_{\text{VI}})^2} \right)^{\frac{3}{2}}. \quad (50)$$

Lemma 3. Under the condition that $N_{\text{CD}} + N_{\text{VI}}$ is large or t_u is small,

- the CDF of T_{ET} is approximated by

$$\hat{F}_{\text{ET}}(x) \approx \begin{cases} \Phi(r_x) + \phi(r_x) \left(\frac{1}{r_x} - \frac{1}{z_x} \right), & x \neq \Psi, \\ \frac{1}{2} + \frac{t_2}{6\sqrt{2\pi}\Upsilon}, & x = \Psi, \end{cases} \quad (51)$$

where

$$r_x = \text{sign}(\Xi_3(x)) \sqrt{2x\Xi_3(x) - 2M(\Xi_3(x))}, \quad \text{and} \quad (52)$$

$$z_x = \Xi_3(x) \sqrt{M''(\Xi_3(x))}.$$

$M(s)$ is given in Eq. (53). $\Xi_3(\cdot)$ is the inverse function of $M'(\cdot)$.

- the PDF of T_{ET} is approximated by

$$\hat{f}_{\text{ET}}(x) \approx \frac{\exp(M(\Xi_3(x)) - x\Xi_3(x))}{\sqrt{2\pi M''(\Xi_3(x))}}, \quad x > 0. \quad (54)$$

$$M(s) = L(s) + \vartheta t_u s + \frac{s^2}{2} \left(\frac{\epsilon_{\text{CD}} N_{\text{CD}} t_u^2}{(1 - \epsilon_{\text{CD}})^2} + \frac{\epsilon_{\text{VI}} N_{\text{VI}} t_u^2}{(1 - \epsilon_{\text{VI}})^2} \right), \quad s < \min \left\{ \frac{\chi_{\text{RA}} \alpha_{\text{RA}}}{n_{\text{ET}} \zeta_c(\kappa)}, \frac{\chi_{\text{MEC}} \alpha_{\text{MEC}} \kappa}{n_{\text{ET}} \zeta_d(\kappa)}, \frac{\chi_{\text{MEC}} \beta_{\text{VI}}}{n_{\text{VI}}} \right\}. \quad (53)$$

Proof: The proof is similar to the proof of Lemma 1. The CGF is shown in Eq. (53). Ψ is the expectation of T_{ET} . It is obvious that $M'(s)$ is an increasing function of s . Thus, the inverse function of $M'(s)$ exists, which we denote by $\Xi_3(\cdot)$. Besides, we find that $M''(0)^{3/2} = \Upsilon$ and $M'''(0) = \iota_2$. Thus, we obtain Eq. (51) according to LR formula [20, Eq. (1.21)]. With the help of the saddlepoint density function [Eqs. (1.4) and (1.5)] [20], we obtain Eq. (54). ■

By combining CLT with SPA, we can directly obtain the CDF of T_{ET} . The same method can be applied to obtaining the CDF of T_1 under the condition that $N_{\text{HL}} + N_{\text{LL}} + N_{\text{CD}} + N_{\text{VI}}$ is large or t_u is small. Let $\tilde{M}(s)$ denote the CGF of T_1 , which is provided in Eq. (55), where $s < \min \left\{ \frac{\chi_{\text{MEC}} \beta_{\text{LL}}}{N_{\text{HL}} n_{\text{HL}}}, \frac{\chi_{\text{RA}} \alpha_{\text{RA}}}{n_{\text{ET}} \zeta_c(\kappa)}, \frac{\chi_{\text{MEC}} \alpha_{\text{MEC}} \kappa}{n_{\text{ET}} \zeta_d(\kappa)}, \frac{\chi_{\text{MEC}} \beta_{\text{VI}}}{n_{\text{ET}}} \right\}$. Besides, we also define $\tilde{\Psi}$ and $\tilde{\Upsilon}$ as follows

$$\tilde{\Psi} = \tilde{\theta} + \left(\vartheta + \frac{N_{\text{HL}}}{1 - \epsilon_{\text{HL}}} + \frac{N_{\text{LL}}}{1 - \epsilon_{\text{LL}}} \right) t_u. \quad (56)$$

$$\tilde{\Upsilon} = \left(\Upsilon^{\frac{2}{3}} + \frac{N_{\text{HL}}^2 n_{\text{HL}}^2 \alpha_{\text{MEC}}}{\chi_{\text{MEC}}^2 \beta_{\text{LL}}^2} + \frac{\epsilon_{\text{CD}} N_{\text{CD}} t_u^2}{(1 - \epsilon_{\text{CD}})^2} + \frac{\epsilon_{\text{VI}} N_{\text{VI}} t_u^2}{(1 - \epsilon_{\text{VI}})^2} \right)^{\frac{3}{2}}. \quad (57)$$

By substituting $\tilde{M}(s)$, $\tilde{\iota}_2$ (defined below Eq. (33)), $\tilde{\Psi}$, and $\tilde{\Upsilon}$ into Eqs. (51) and (54), we can obtain $\hat{F}_{T_1}(x)$ and $\hat{f}_{T_1}(x)$, where $\hat{F}_{T_1}(x)$ and $\hat{f}_{T_1}(x)$ are the continuous approximation for the CDF and PDF of T_1 , respectively. We then present the continuous approximation for the CDF of T in Theorem 2.

Theorem 2. Under the condition that $N_{\text{HL}} + N_{\text{LL}} + N_{\text{CD}} + N_{\text{VI}}$ is large or t_u is small, the CDF of the closed-loop latency is approximated by

$$\hat{F}_T(x) \approx \mathbb{I}\{x > \tau_{\text{PF}}\} F_{\text{CL}}(x - \tau_{\text{PF}}) \hat{F}_{T_1}(x). \quad (58)$$

Note that if $N_{\text{LL}} + N_{\text{HL}}$ is large or t_u is small, we can also use the continuous approximation $\hat{F}_{\text{CL}}(x)$ to substitute $F_{\text{CL}}(x)$ in Eq. (58). However, N_{LL} is usually equal to 1 in practical scenarios. Besides, T_{CL} consists of only three latency components, among which the CDF of $T_{\text{LL}}^{\text{cp}}$ is known. Thus, we employ the general approximation for the CDF of T_{CL} in Eq. (58) to ensure high accuracy while maintaining efficiency.

C. Efficient Evaluation for Different Kinds of Constraints and Properties for Optimization

In this subsection, we will propose the methods for efficiently evaluating some kinds of constraints with the help of conclusions in Sections IV-A and IV-B. Then, we will present some properties of the communication and computation processes in this system, which are useful for further optimization.

In Sections IV-A and IV-B, we have derived the CDFs of T_{CL} , T_{ET} , T_{FL} , and T . Besides, the expectation and

variance of each latency component are known. Thus, all constraints mentioned in Section II-B can be characterized by these conclusions. However, certain constraints can be evaluated more efficiently, prompting us to present the efficient evaluating methods based on the SPA-based methods.

Eq. (9) imposes a constraint on the conditional expectation $\mathbb{E} \left\{ (T_{\text{ET}} - \tau_{\text{PF}})^+ \right\}$. An intuitive approach to calculate this would be to use the PDF of T_{ET} . However, we can not obtain the PDF of T_{ET} for general cases since T_{ET} may not be a continuous random variable. While it appears feasible to derive $f_{\text{ET}}(x)$ by Eq. (54) under the assumption that $N_{\text{CD}} + N_{\text{VI}}$ is large or t_u is small, the closed-form expression of $\Xi_3(x)$ in Eq. (54) is hard to obtain. This complication makes the computation of $f_{\text{ET}}(x)$ over a continuous interval impractical. One potential method to approximate the PDF of T_{ET} is through discretization, as used in our previous work [22].

Though we can design a discrete approximation for the PDF of T_{ET} based on Lemma 3, it is computationally intensive due to the need to solve SPA equations at numerous points when granularity is small. Therefore, we present an efficient method to derive $\mathbb{E} \left\{ (T_{\text{ET}} - \tau_{\text{PF}})^+ \right\}$ in Corollary 1.

Corollary 1. Under the condition that $N_{\text{CD}} + N_{\text{VI}}$ is large or t_u is small, $\mathbb{E} \left\{ (T_{\text{ET}} - \tau_{\text{PF}})^+ \right\}$ can be approximated by Eq. (58), where $\hat{F}_{\text{ET}}(\tau_{\text{PF}})$, $\hat{f}_{\text{ET}}(\tau_{\text{PF}})$, and $\Xi_3(\tau_{\text{PF}})$ are given in Lemma 3.

Proof: Corollary 1 is based on the Eq. (2) in [36]. Note that Eq. (2) in [36] requires that the random variable should be continuous. As we analyzed before Lemma 3, $T_{\text{CD}}^{\text{cm}} + T_{\text{VI}}^{\text{cm}}$ can be approximated by a normal random variable by CLT under the condition that $N_{\text{CD}} + N_{\text{VI}}$ is large or t_u is small. By this means, T_{ET} can be treated as a continuous random variable with CDF $\hat{F}_{\text{ET}}(\tau_{\text{PF}})$ and $\hat{f}_{\text{ET}}(\tau_{\text{PF}})$. ■

Based on Eq. (58) in Corollary 1, we can evaluate $\mathbb{E} \left\{ (T_{\text{ET}} - \tau_{\text{PF}})^+ \right\}$ by only calculating the CDF and PDF of T_{ET} at a single point, which is more efficient than the discrete approximation method.

Then, we turn our focus to Eq. (11). The communication latency of PF data is stochastic for this constraint. To calculate $\Pr\{|T_{\text{ET}} - T_{\text{PF}}| < \tau_{\text{td}}\}$, it is equivalent to calculate

$$\Pr\{T_{\text{ET}} - T_{\text{PF}} < \tau_{\text{td}}\} - \Pr\{T_{\text{ET}} - T_{\text{PF}} < -\tau_{\text{td}}\}. \quad (59)$$

Thus, we can employ a similar method proposed in Theorem 1 to adopt the SPA-based method by first deriving the CGF of $T_{\text{ET}} - T_{\text{PF}}$. Due to space limits, we omit the details.

Then, we provide some useful properties for optimizing the system's performance. For the PF data, we present a conclusion on the period allocation for the case with CSIRT and FSD to minimize the average power consumption for the

$$\tilde{M}(s) = M(s) - \alpha_{\text{MEC}} \ln \left(1 - \frac{N_{\text{HL}} n_{\text{HL}} s}{\chi_{\text{MEC}} \beta_{\text{LL}}} \right) + \left(\frac{N_{\text{HL}} t_u}{1 - \epsilon_{\text{HL}}} + \frac{N_{\text{LL}} t_u}{1 - \epsilon_{\text{LL}}} \right) s + \frac{s^2}{2} \left(\frac{\epsilon_{\text{HL}} N_{\text{HL}} t_u^2}{(1 - \epsilon_{\text{HL}})^2} + \frac{\epsilon_{\text{LL}} N_{\text{LL}} t_u^2}{(1 - \epsilon_{\text{LL}})^2} \right). \quad (55)$$

$$\mathbb{E} \left\{ (T_{\text{ET}} - \tau_{\text{PF}})^+ \right\} \approx (\theta + \vartheta t_u - \tau_{\text{PF}}) \left(1 - \hat{F}_{\text{ET}}(\tau_{\text{PF}}) \right) + \frac{\tau_{\text{PF}} - \theta - \vartheta t_u}{\Xi_3(\tau_{\text{PF}})} \hat{f}_{\text{ET}}(\tau_{\text{PF}}), \quad \text{if } \tau_{\text{PF}} \neq \theta + \vartheta t_u. \quad (58)$$

PF data transmission. For the ET data, we offer a conclusion related to the choice of compression ratio. For convenience, we let

$$\varphi_j = \left[\frac{N_0 B_{\text{PF}}}{c_1 d_j^{-\ell_j}} \left(2^{\frac{n_{\text{PF}}}{T_s B_{\text{PF}}}} - 1 \right) \right]^{-\frac{1}{c_3+1}}, \quad j \in \{\text{PF1}, \text{PF2}\}. \quad (60)$$

Lemma 4. Given that the transmission of PF data with CSIRT and FSD, the period allocation to achieve a minimum $P_{\text{PF1}} + P_{\text{PF2}}$ is $\tau_{\text{PF1}} = \frac{\tau_{\text{PF}} \varphi_{\text{PF2}}}{\varphi_{\text{PF1}} + \varphi_{\text{PF2}}}$ and $\tau_{\text{PF2}} = \frac{\tau_{\text{PF}} \varphi_{\text{PF1}}}{\varphi_{\text{PF1}} + \varphi_{\text{PF2}}}$.

Proof: See Appendix C. ■

Lemma 5. For $\zeta_d(\kappa)$ satisfying Eq. (23) with $\psi \geq 1$ and (24) with $\omega_7 > 1 + \frac{\omega_8}{\omega_6}$, $\frac{\kappa}{\zeta_d(\kappa)}$ is a decreasing function of κ . For $\zeta_d(\kappa)$ shown in Eq. (24) with $\omega_7 \leq 1$, $\frac{\kappa}{\zeta_d(\kappa)}$ is an increasing function of κ .

Proof: See Appendix D. ■

In Lemma 4, we provide a closed-form resource allocation scheme for the transmission of PF data. In Lemma 5, we present conclusions regarding the monotonic properties of $\frac{\kappa}{\zeta_d(\kappa)}$. These conclusions offer guidance for the optimization in the next subsection.

D. A Specific Optimization Problem

In this subsection, we will show a specific case of Problem (25) and demonstrate how to solve this problem with the help of the proposed theorems and lemmas.

For simplicity, we consider optimizing the compression ratio κ and transmission power P_{PF1} , P_{PF2} , and P_{CD} , while treating the bandwidth and other transmission powers as fixed. By adopting the constraints from vertex 8 in Fig. 3, the optimization problem is formulated as

$$\min_{\kappa, P_{\text{PF1}}, P_{\text{PF2}}, P_{\text{CD}}} \epsilon \Pr\{T > T_{\text{th}}\} + \frac{1-\epsilon}{P_{\text{max}}} (P_{\text{PF1}} + P_{\text{PF2}} + P_{\text{CD}}) \quad (61a)$$

$$\text{s.t.} \quad \tau_{\text{PF1}} + \tau_{\text{PF2}} \leq \tau_{\text{PF}}, \quad (61a)$$

$$\Pr\{T_{\text{ET}} < \tau_{\text{PF}}\} \geq \eta_{\text{ts}}, \quad (61b)$$

$$\text{Var}\{T_{\text{ET}} - \tau_{\text{PF}}\} \leq \rho_{\text{ts}}, \quad (61c)$$

$$R_{\text{CD}} = \frac{t_u n_{\text{CD}}^{(1)}}{\kappa}, \quad (61d)$$

$$\zeta_c(\kappa) = \exp(\psi \kappa) - \exp(\psi), \quad (61e)$$

$$\zeta_d(\kappa) = \omega_0 (\exp(\psi \kappa) - \exp(\psi)), \quad (61f)$$

where $\psi \geq 1$. $n_{\text{CD}}^{(1)}$ represents the packet size of the compressed data when $\kappa = 1$. Eq. (61d) means that we change the size of a compressed-data packet to fix N_{CD} . In this problem, $d(T) = \Pr\{T > T_{\text{th}}\}$ represents the aim to reduce the delay violation probability with threshold T_{th} for the closed-loop latency. $P_{\text{max}} \geq P_{\text{PF1}} + P_{\text{PF2}} + P_{\text{CD}}$ is used to normalize the power-related term in the optimization objective.

Then, we provide the analysis for this optimization problem. According to Eq. (15), Eq. (61c) is equivalent to

$$\xi_{\text{ET}}^c + \xi_{\text{ET}}^d + \xi_{\text{VI}}^{\text{cp}} + \frac{\epsilon_{\text{CD}} N_{\text{CD}} t_u^2}{(1-\epsilon_{\text{CD}})^2} + \frac{\epsilon_{\text{VI}} N_{\text{VI}} t_u^2}{(1-\epsilon_{\text{VI}})^2} \leq \rho_{\text{ts}}, \quad (62)$$

where ξ_{ET}^c , ξ_{ET}^d , and $\xi_{\text{VI}}^{\text{cp}}$ are defined in Section III. Both ξ_{ET}^c and ξ_{ET}^d are functions of κ . According to Lemma 5, $\xi_{\text{ET}}^c + \xi_{\text{ET}}^d$

is an increasing function of κ with $\psi \geq 1$. Thus, we can determine an upper bound of κ through Eq. (62), which we denote as $\hat{\kappa}_1$. $\hat{\kappa}_1$ is the solution of the following equation, which can be solved efficiently through binary search.

$$\xi_{\text{ET}}^c + \xi_{\text{ET}}^d = \rho_{\text{ts}} - \xi_{\text{VI}}^{\text{cp}} - \frac{\epsilon_{\text{CD}} N_{\text{CD}} t_u^2}{(1-\epsilon_{\text{CD}})^2} - \frac{\epsilon_{\text{VI}} N_{\text{VI}} t_u^2}{(1-\epsilon_{\text{VI}})^2}. \quad (63)$$

Given τ_{PF} , the optimal choice of τ_{PF1} and τ_{PF2} for minimizing $P_{\text{PF1}} + P_{\text{PF2}}$ are determined by Lemma 4. By substituting $\tau_{\text{PF1}} = \frac{\tau_{\text{PF}} \varphi_{\text{PF2}}}{\varphi_{\text{PF1}} + \varphi_{\text{PF2}}}$ and $\tau_{\text{PF2}} = \frac{\tau_{\text{PF}} \varphi_{\text{PF1}}}{\varphi_{\text{PF1}} + \varphi_{\text{PF2}}}$ into Eq. (17), we have

$$P_{\text{PF1}} + P_{\text{PF2}} = c_2 \left(\varphi_{\text{PF1}}^{-c_3-1} + \varphi_{\text{PF2}}^{-c_3-1} \right) + \left(\frac{\tau_{\text{PF}} \varphi_{\text{PF1}} \varphi_{\text{PF2}}}{\varphi_{\text{PF1}} + \varphi_{\text{PF2}}} \right)^{-c_3} \left(\varphi_{\text{PF1}}^{-1} + \varphi_{\text{PF2}}^{-1} \right). \quad (64)$$

For P_{CD} , we can express it as a function of κ . Based on Eqs. (7) and (61d), we have

$$P_{\text{CD}} = \frac{-N_0 B_{\text{CD}}}{d_{\text{RB}}^{-\ell_{\text{CD}}} \ln(1-\epsilon_{\text{CD}})} \left(2^{\frac{t_u n_{\text{CD}}^{(1)}}{B_{\text{CD}} \cdot \kappa} - 1} \right). \quad (65)$$

For the objective function and Eq. (61b), we adopt the SPA approximation in Theorem 1. We start our analysis with Eq. (61b). Since the distribution of transmission time is fixed in this problem, our focus is on the computation, compression, and decompression time. In this case, the value of κ will influence $\Pr\{T_{\text{ET}} < \tau_{\text{PF}}\}$ through changing the distribution of $T_{\text{ET}}^c + T_{\text{ET}}^d + T_{\text{VI}}^{\text{cp}}$. Since in Lemma 5 we have proved that $\frac{\kappa}{\zeta_d(\kappa)}$ is a decreasing function of κ with $\Psi \geq 1$, the CDF of $T_{\text{ET}}^c + T_{\text{ET}}^d + T_{\text{VI}}^{\text{cp}}$ is a decreasing function of κ . Thus, the SPA $F_1(\tau_{\text{PF}})$ can be seen as a decreasing function of κ . Therefore, we can obtain another upper bound of κ through Eq. (61b), which we denote by $\hat{\kappa}_2$. Combining $\hat{\kappa}_2$ with $\hat{\kappa}_1$ and κ_{max} , the upper bound of κ is given by $\kappa \leq \min\{\kappa_{\text{max}}, \hat{\kappa}_1, \hat{\kappa}_2\}$.

Similarly, $\Pr\{T > T_{\text{th}}\}$ is an increasing function of κ . Therefore, there is a tradeoff between $\Pr\{T > T_{\text{th}}\}$ and $P_{\text{PF1}} + P_{\text{PF2}} + P_{\text{CD}}$ since P_{CD} is a decreasing function of κ as shown in Eq. (65). In contrast to the grid search used in [8], we can utilize the gradient-based method to find the near-optimal solution to Problem (61) thanks to the analytical expressions obtained from SPA. Since the convexity of $\Pr\{T > T_{\text{th}}\}$ is unknown, we can adopt the gradient-descent method with random start points to relieve the probability of obtaining the local optimal solutions. It is an important future work to consider more advanced algorithms for solving this problem, which is beyond the scope of this paper. Besides, through the numerical results shown in Section V, we find that the objective function of Problem (61) is a unimodal function of κ . Therefore, we can use ternary search [37] to find the optimal solution. Let N denote the number of feasible searching points. The computational complexity of the ternary search is $O(\log_3 N)$ [37], which is lower than that of the grid search.

We can use the numerical gradient to approximately obtain the gradient information. Moreover, we can also try to characterize the analytical gradient since we have the analytical expression of the latency distribution. To use the gradient-based method, we need to show the existence of $\frac{\partial \Pr\{T > T_{\text{th}}\}}{\partial \kappa}$. According to Theorem 1, it is equivalent to show the existence

of $\frac{\partial \tilde{F}_1(x)}{\partial \kappa}$. We divide the following discussion into three parts. We first discuss $\frac{\partial s^*}{\partial \kappa}$, where s^* is the solution to the saddlepoint function of $\tilde{F}_1(x)$. The saddlepoint equation of $\tilde{F}_1(x)$ is given by $\tilde{L}'(s^*) = x$, where $\tilde{L}'(\cdot)$ is also a function of κ . By adopting implicit differential, we can obtain $\frac{\partial s^*}{\partial \kappa}$ from the saddlepoint equation. For the simplicity of expression, we let $s^* = Z(\kappa)$ denote the solution of the saddlepoint equation. With abuse of notations, we denote the CGF by $\tilde{L}(\kappa, s^*)$ in the following discussion. Then, we discuss $\frac{du_x}{d\kappa}$. For the simplicity of expression, we let $\Omega_0(\kappa) = \tilde{L}(\kappa, s^*)|_{s^*=Z(\kappa)}$, $\Omega_1(\kappa) = \frac{\partial \tilde{L}(\kappa, s^*)}{\partial s^*}|_{s^*=Z(\kappa)}$ and $\Omega_2(\kappa) = \frac{\partial^2 \tilde{L}(\kappa, s^*)}{\partial (s^*)^2}|_{s^*=Z(\kappa)}$. According to Eq. (30), we obtain that

$$\frac{du_x}{d\kappa} = \sqrt{\Omega_2(\kappa)} \cdot \frac{dZ(\kappa)}{d\kappa} + \frac{Z(\kappa)}{2\sqrt{\Omega_2(\kappa)}} \cdot \frac{d\Omega_2(\kappa)}{d\kappa}. \quad (66)$$

Finally, we discuss $\frac{dv_x}{d\kappa}$. According to Eq. (30), we have

$$v_x dv_x = \left(x \frac{dZ(\kappa)}{d\kappa} - \frac{d\Omega_0(\kappa)}{d\kappa} \right) d\kappa. \quad (67)$$

Based on Eq. (67), we have

$$\frac{dv_x}{d\kappa} = \frac{x \frac{dZ(\kappa)}{d\kappa} - \frac{d\Omega_0(\kappa)}{d\kappa}}{\text{sign}(Z(\kappa)) \sqrt{2xZ(\kappa) - 2\Omega_0(\kappa)}}. \quad (68)$$

Based on Eqs. (67) and (68), we can perform optimization by using gradient-based method. It remains open to show whether $\frac{dv_x}{d\kappa}$ is bounded when $Z(\kappa) \rightarrow 0$. At least we can use the clipped gradient in the gradient-descent method.

V. SIMULATION AND NUMERICAL RESULTS

In this section, we validate the proposed framework through Monte Carlo simulations and numerical results. The parameters of the simulation and numerical calculations are mainly based on [8] and [34]. Specifically, we set $\alpha_{\text{MEC}} = 1.25$, $\alpha_{\text{RA}} = 1.5$, $\beta_{\text{LL}} = \beta_{\text{VI}} = 1$, $N_{\text{HL}} = 3$, $N_{\text{LL}} = 1$, $n_{\text{HL}} = 128$ KB, $\epsilon_{\text{HL}} = \epsilon_{\text{LL}} = 10^{-5}$, $\chi_{\text{RA}} = 5$ GHz, $\chi_{\text{MEC}} = 15$ GHz, $\Delta = 10^{-5}$, and $n_{\text{ET}} = 1$ MB. $\zeta_c(\kappa)$ and $\zeta_d(\kappa)$ follow Eq. (22) and Eq. (23), respectively, with $\psi = 3.5$ and $\omega_0 = 0.1$.

In Figs. 5-8, we present the simulation and numerical results of CDFs of T_{ET} and T . The simulation and numerical results of the CDF of T_{CL} are provided in Figs. 9 and 10. In these figures, we let $N_{\text{CD}}^{(1.1)}$ denote the number of compressed-data packets with $\kappa = 1.1$. Thus, the number of compressed-data packets with $\kappa = 1.2$ is given by $N_{\text{CD}}^{(1.2)} = \left\lceil \frac{1.1}{1.2} N_{\text{CD}}^{(1.1)} \right\rceil$. The curves with the legend ‘Simulation’ refer to the Monte-Carlo simulation results averaged over 10^7 independent simulations, while the curves with the legend ‘Theorem 1’, ‘Lemma 3’, and ‘Theorem 2’ represent the numerical results of Alg. 1, Eq. (51), and Eq. (58), respectively. We considered four scenarios in Figs. 5-8. Fig. 5 represents the general scenario. Fig. 6 represents the scenario with a large number of packets. Fig. 7 represents the scenarios with a small t_u and a small number of packets. Fig. 8 represents the extreme scenario in which the number of packets is small and t_u is large. By comparing the simulation and numerical results, we find that both Theorem 1, Lemma 3, and Theorem 2 perform well in Figs. 5, 6, and 7. However, Theorem 1 significantly outperforms Lemma

3 in Fig. 8(a) and Theorem 2 in Fig. 8(c). The results in these four figures validate the accuracy of Theorem 1. When $\Pr\{T > x\} = 0.01$, the absolute errors by adopting the approximation method in Theorem 1 are on the order of 10^{-5} in Figs. 5-7 and is on the order of 10^{-4} in Fig. 8, which are at least two orders of magnitude smaller than 0.01. Besides, as we analyzed in Section IV, Lemma 3 can be applied when t_u is small or the number of packets is large. The results in Figs. 5, 6, and 7 show the effectiveness of Lemma 3 and Theorem 2. The reason that Lemma 3 and Theorem 2 do not perform well in Fig. 8 is that the discrete components of T_{ET} and T are dominant, which is evident from the simulation curves in Fig. 8. Under this condition, using CLT to conduct continuous approximation leads to bad performance. In summary, Theorem 1 provides high accuracy in most closed-loop scenarios. Except for the extreme scenario where the number of packets is small or the transmission time of one packet is large, Lemma 3 and Theorem 2 offer satisfying accuracy. The high accuracy of Theorem 1 makes it capable of satisfying the specified constraint by setting the constraint stricter. It is an important future work to theoretically prove the robustness of the SPA-based method used in optimization problems.

Several intriguing details emerge from our analysis. First, we find that Theorem 2 seems to perform better than Theorem 1 in some points. This phenomenon may arise from the threshold Δ set in Alg. 1, which limited the precision of the results. Second, as shown in Fig. 8, the curves of Theorem 1 match well with those of the simulation results. This result shows the universality of Theorem 1 even in extreme scenarios. Moreover, we observe that the CDF does not always decrease with an increase in κ , as illustrated in Figs. 6(a) and 6(c). This behavior complicates the determination of the optimal compression ratio since the CDF with a given threshold x is not monotonic with respect to κ . However, when x is large (e.g., when $1 - \Pr\{T_{\text{ET}} < x\}$ is small), the CDF tends to decrease as κ increases. Since we mainly focus on the threshold with which $1 - \Pr\{T_{\text{ET}} < x\}$ is small, it is important to identify and prove the condition under which $1 - \Pr\{T_{\text{ET}} < x\}$ decreases with increasing κ for a given x in future work.

We then present the simulation and numerical results of $\mathbb{E}\{(T_{\text{ET}} - \tau_{\text{PF}})^+\}$ in Fig. 11. The parameter settings in Figs. 11(a)-(d) are identical with those in Figs. 5-8. The curves with the legend ‘Simulation’ refer to the Monte-Carlo simulation results averaged over 10^7 independent simulations, while the curves with the legend ‘Corollary 1’ represent the numerical results of Eq. (58). Notably, the numerical results closely match the simulation results in Fig. 11(b), confirming the effectiveness of Corollary 1. Moreover, the numerical results in Figs. 11(a) and 11(c) also demonstrate satisfactory performance. However, the difference between the numerical and simulation results becomes obvious in Fig. 11(d). In this extreme scenario, generalization of Eq. (58) is required to achieve an efficient and accurate approximation for the conditional expectation, which is an important future work.

Finally, we present the numerical results of solving the opti-

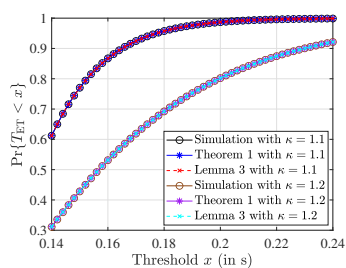
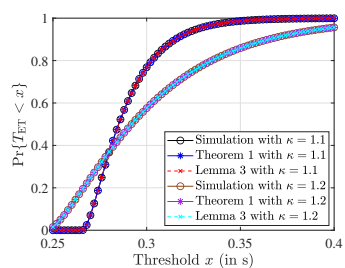
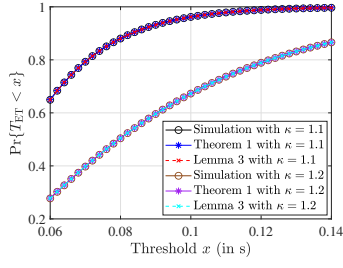
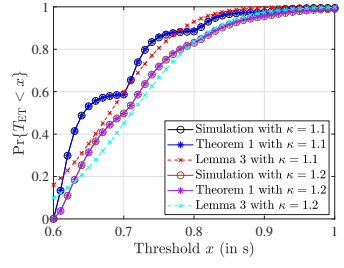
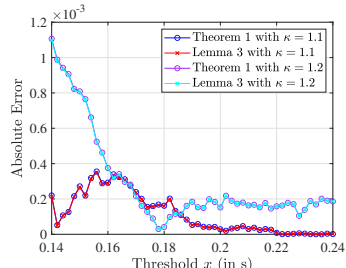
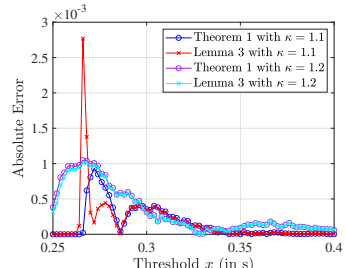
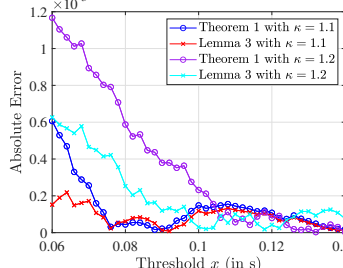
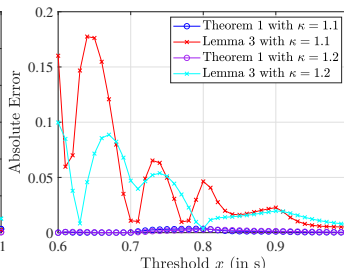
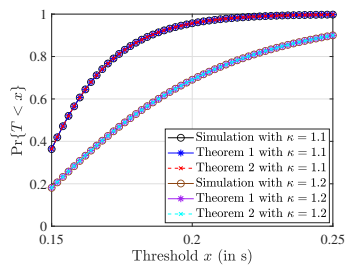
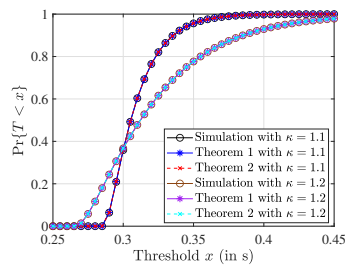
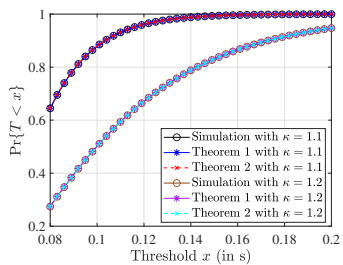
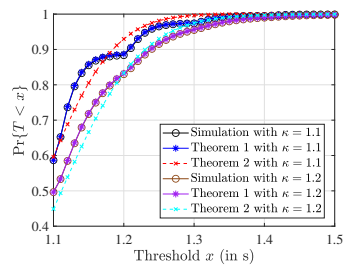
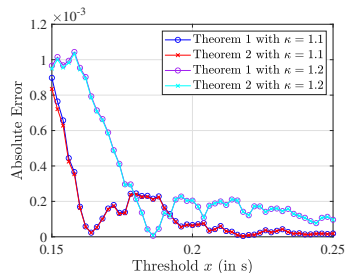
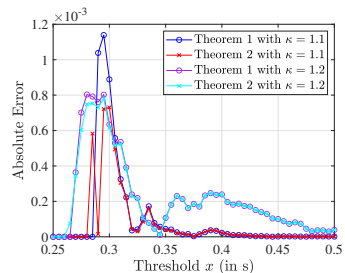
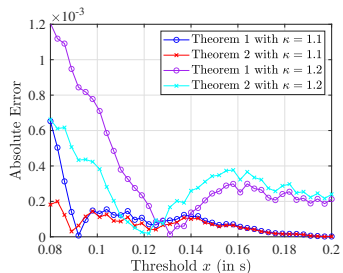
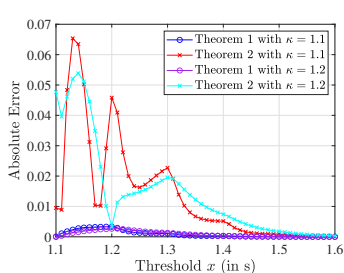
(a) CDF of T_{ET} .(a) CDF of T_{ET} .(a) CDF of T_{ET} .(a) CDF of T_{ET} .(b) Approximation error of T_{ET} .(b) Approximation error of T_{ET} .(b) Approximation error of T_{ET} .(b) Approximation error of T_{ET} .(c) CDF of T .(c) CDF of T .(c) CDF of T .(c) CDF of T .(d) Approximation error of T (d) Approximation error of T (d) Approximation error of T (d) Approximation error of T

Fig. 5. T_{ET} and T with $t_u = 5$ ms, $N_{CD}^{(1,1)} = 20$, $N_{VI} = 3$, $\epsilon_{CD} = 10^{-3}$, and $\epsilon_{VI} = 10^{-4}$.

Fig. 6. T_{ET} and T with $t_u = 5$ ms, $N_{CD}^{(1,1)} = 50$, $N_{VI} = 3$, $\epsilon_{CD} = 10^{-3}$, and $\epsilon_{VI} = 10^{-4}$.

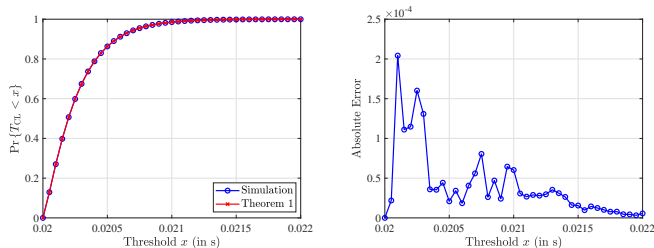
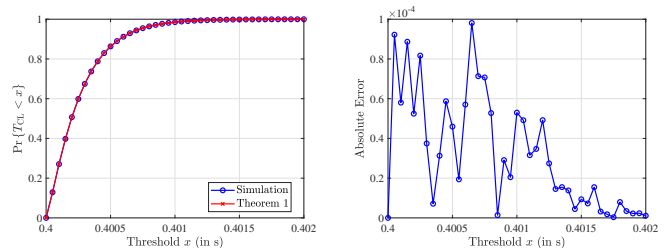
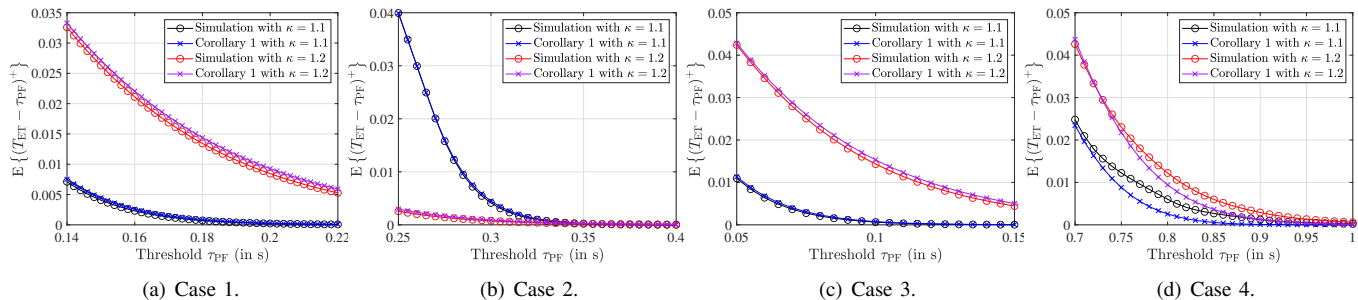
Fig. 7. T_{ET} and T with $t_u = 5$ ms, $N_{CD}^{(1,1)} = 5$, $N_{VI} = 1$, $\epsilon_{CD} = 10^{-1}$, and $\epsilon_{VI} = 10^{-3}$.

Fig. 8. T_{ET} and T with $t_u = 100$ ms, $N_{CD}^{(1,1)} = 5$, $N_{VI} = 1$, $\epsilon_{CD} = 10^{-1}$, and $\epsilon_{VI} = 10^{-3}$.

mization problems outlined in Section IV-D. Unless otherwise specified, the system parameters of Figs. 12 and 13 are the same as those in Fig. 5. We set $(N_0 B_j)/d_j^{-\ell_j} = 1$ in Figs. 12 and 13. Given τ_{PF} , P_{max} is set as the sum of $P_{PF1} + P_{PF2}$ satisfying Eq. (64) and P_{CD} with $\kappa = 1$. By this means, the power term in Problem (61) is normalized.

In Fig. 12, we show the value of the objective function of Problem (61) versus the compression ratio κ . The solid curves in Fig. 12 represent the results of grid search with granularity 10^{-4} . We find that the objective function is unimodal with respect to κ , as shown in Fig. 12. Therefore, we adopt the ternary search to find the minimum points, which are marked

by circles in Fig. 12. The minimum points obtained by grid search are marked by “*” in Fig. 12. The results of the ternary search match well with those of the grid search, indicating that advanced algorithms may efficiently solve this problem. Besides, $\varepsilon = 1$ in Fig. 12(a) refers to the case in which the objective function is $\Pr\{T > T_{th}\}$. We see that under the given system parameters, $\Pr\{T > T_{th}\}$ is a convex function of κ . Since the power term in the objective function of Problem (61) is also a convex function of κ , the overall objective function of Problem (61) is a convex function of κ . It is an important future work to characterize the conditions under which the optimization problem is convex. Moreover,

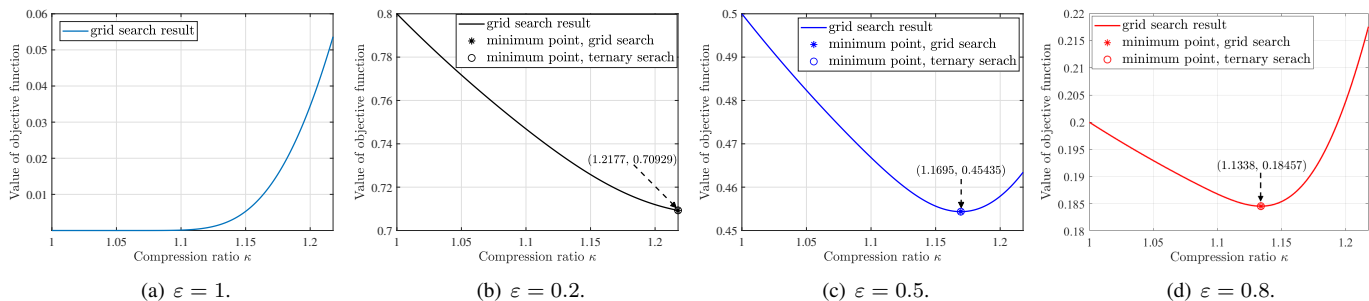
(a) CDF of T_{CL} .(b) Approximation error of T_{CL} .Fig. 9. T_{CL} with $t_u = 5$ ms.(a) CDF of T_{CL} .(b) Approximation error of T_{CL} .Fig. 10. T_{CL} with $t_u = 100$ ms.

(a) Case 1.

(b) Case 2.

(c) Case 3.

(d) Case 4.

Fig. 11. Approximation of $\mathbb{E}\{(T_{ET} - \tau_{PF})^+\}$ versus τ_{PF} .(a) $\varepsilon = 1$.(b) $\varepsilon = 0.2$.(c) $\varepsilon = 0.5$.(d) $\varepsilon = 0.8$.Fig. 12. Value of the objective function versus the compression ratio κ with $\tau_{PF} = 0.25$ s and $T_{th} = 0.3$ s.

the results in Fig. 12 show that the optimal κ decreases with the increase of ε . This is because $\Pr\{T > T_{th}\}$ is an increasing function of κ and the power term is a decreasing function of κ . With a larger ε , the weight of $\Pr\{T > T_{th}\}$ becomes higher, leading to the decrease of κ .

From the analysis of Fig. 12, we see that there exists an optimal value of κ , highlighting a tradeoff between the performance of latency and power in the considered system. In Fig. 13, we present the power-latency tradeoff with different τ_{PF} . Note that the feasible interval of κ is influenced by the value of τ_{PF} . Thus, the tradeoff curves have varying ranges as shown in Fig. 13. From Fig. 13, we find that the optimal power-latency tradeoff is convex in the considered system. As shown in Fig. 13, the power consumption is higher with a smaller τ_{PF} when achieving the same latency violation probability. This is because a smaller τ_{PF} refers to a larger $P_{PF1} + P_{PF2}$ according to Eq. (64). Besides, a smaller τ_{PF} imposes stricter requirements on the ET latency, which results in a larger P_{CD} . These results may provide instructions for the choices of system parameters.

VI. CONCLUSION

In this paper, we focused on formulating a unified timing-analysis framework and proposing a general method to characterize the distribution of the closed-loop timing performance in CGC systems. The multi-modal feedback was divided into PF and ET data due to the heterogeneity of the feedback mechanism. Covering timeliness, jitter, and reliability, we developed a unified framework of timing analysis for CGC systems with various configurations, which includes both average-based and tail-based constraints. The randomness of computation, compression, and communication were incorporated into the closed-loop timing analysis. To address the difficulties resulting from the sum of multiple random latency components, an SPA-based method was conceived, which helped us derive the analytical expression of the closed-loop latency and other timing metrics. Important future topics include further optimization based on this unified framework, the introduction of emerging timing metrics into this framework, and the generalization of the approximation for the conditional expectation of timing metrics.

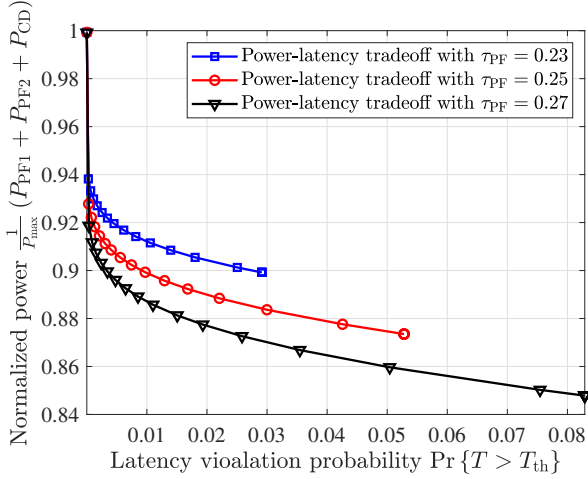


Fig. 13. Power-latency tradeoff in the considered system.

APPENDIX A PROOF OF LEMMA 1

The essence of the proof is to use the LR formula [20, Eq. (1.21)]. For a detailed derivation of the LR formula, please refer to [20, Ch. 2]. Here we give the sketch of how to use Eq. (1.21) of [20]. We first obtain the cumulant generating function (CGF) of $T_{\text{ET}}^c + T_{\text{ET}}^d + T_{\text{VI}}^{\text{cp}}$. The CGF of gamma random variable $X_1 \sim \text{Gamma}(\alpha, \beta)$ is given by

$$K_{X_1}(s) = -\alpha \ln \left(1 - \frac{s}{\beta} \right), \quad s < \beta. \quad (69)$$

Based on Eq. (69), we obtain the CGF of $T_{\text{ET}}^c + T_{\text{ET}}^d + T_{\text{VI}}^{\text{cp}}$, which is given in Eq. (31), where $s < \min \left\{ \frac{\chi_{\text{RA}} \alpha_{\text{RA}}}{n_{\text{ET}} \zeta_c(\kappa)}, \frac{\chi_{\text{MEC}} \alpha_{\text{MEC}} \kappa}{n_{\text{ET}} \zeta_d(\kappa)}, \frac{\chi_{\text{MEC}} \beta_{\text{VI}}}{n_{\text{ET}}} \right\}$. To obtain the CDF of $T_{\text{ET}}^c + T_{\text{ET}}^d + T_{\text{VI}}^{\text{cp}}$, we need to solve the saddlepoint equation to obtain the saddlepoint s_x . The saddlepoint equation is given by $L'(s_x) = x$, where $L'(s)$ is given by

$$L'(s) = \frac{\alpha_{\text{RA}}}{\frac{\chi_{\text{RA}} \alpha_{\text{RA}}}{n_{\text{ET}} \zeta_c(\kappa)} - s} + \frac{\alpha_{\text{MEC}}}{\frac{\chi_{\text{MEC}} \alpha_{\text{MEC}} \kappa}{n_{\text{ET}} \zeta_d(\kappa)} - s} + \frac{\alpha_{\text{MEC}}}{\frac{\chi_{\text{MEC}} \beta_{\text{VI}}}{n_{\text{ET}}} - s}. \quad (70)$$

$L'(s_x)$ is an increasing function of s_x . Thus, the inverse function of $L' : s_x \mapsto x$ exists, which is denoted by $\Xi_1 : x \mapsto s_x$. There is a unique solution of the saddlepoint equation, i.e., $\Xi_1(x)$, which can be solved by binary search.

Then, we divide the following proof into two cases. Let $\theta = \mathbb{E}\{T_{\text{ET}}^c + T_{\text{ET}}^d + T_{\text{VI}}^{\text{cp}}\}$ as shown in (28). The first case is that $x \neq \theta$ holds. According to the LR formula [20, Eq. (1.21)], we obtain

$$F_1(x) = \Phi(v_x) + \phi(v_x) \left(\frac{1}{v_x} - \frac{1}{u_x} \right), \quad (71)$$

where $v_x = \text{sign}(s_x) \sqrt{2(xs_x - L(s_x))}$, and $u_x = s_x \sqrt{L''(s_x)}$. The second-order derivative of $L(s)$ is given by

$$L''(s) = \frac{\alpha_{\text{RA}}}{\left(\frac{\chi_{\text{RA}} \alpha_{\text{RA}}}{n_{\text{ET}} \zeta_c(\kappa)} - s \right)^2} + \frac{\alpha_{\text{MEC}}}{\left(\frac{\chi_{\text{MEC}} \alpha_{\text{MEC}} \kappa}{n_{\text{ET}} \zeta_d(\kappa)} - s \right)^2} + \frac{\alpha_{\text{MEC}}}{\left(\frac{\chi_{\text{MEC}} \beta_{\text{VI}}}{n_{\text{ET}}} - s \right)^2}. \quad (72)$$

Thus, by substituting Eqs. (31) and (72) into the expressions of v_x and u_x , we obtain the first expression in Eq. (29).

The second case is that $x = \theta$ holds. According to the LR formula [20, Eq. (1.21)], $\Pr\{T_{\text{ET}} < \theta\}$ is given by

$$F_1(x) = \frac{1}{2} + \frac{L'''(0)}{6\sqrt{2\pi}L''(0)^{3/2}}. \quad (73)$$

We let $\iota_1 = L''(0)^{3/2}$ and $\iota_2 = L'''(0)$, which are given in Eqs. (26) and (27), respectively. By substituting Eqs. (26) and (27) into Eq. (73), we obtain Eq. (29).

For the PDF, we adopt the saddlepoint density functions in [Eqs. (1.4) and (1.5)] [20]. For a detailed derivation of saddlepoint density functions, please refer to [20, Ch. 2]. By substituting Eqs. (31) and (72) into the Eqs. (1.4) and (1.5) of [20], we obtain Eq. (32).

APPENDIX B PROOF OF LEMMA 2

Similar to the proof of Lemma 1, we shall first obtain the CGF of $T_{\text{CD}}^{\text{cm}} + T_{\text{VI}}^{\text{cm}}$. The CGF of negative binomial random variable $X_2 \sim \text{NB}(N, p)$ is given by

$$K_{X_2}(s) = N(s + \ln p - \ln(1 - (1-p)e^s)), \quad (74)$$

where $s < -\ln(1-p)$. Based on Eq. (74), we obtain the CGF of $T_{\text{CD}}^{\text{cm}} + T_{\text{VI}}^{\text{cm}}$, which is given by Eq. (38). The first-order derivative of $J(s)$ is thus given by

$$J'(s) = \frac{N_{\text{CD}}}{1 - \epsilon_{\text{CD}}e^s} + \frac{N_{\text{VI}}}{1 - \epsilon_{\text{VI}}e^s}, \quad (75)$$

where $s < \min\{-\ln \epsilon_{\text{CD}}, -\ln \epsilon_{\text{VI}}\}$. The saddlepoint equation is thus given by $J'(s_k) = k$. $J'(s_k)$ is an increasing function of s_k . Thus, the inverse function of $J' : s_k \mapsto x$ exists, which is denoted by $\Xi_2 : x \mapsto s_k$. The solution of the saddlepoint equation is thus given by $\Xi_2(k)$.

Based on Eq. (75), we can also obtain

$$J''(s) = \frac{\epsilon_{\text{CD}} N_{\text{CD}} e^s}{(1 - \epsilon_{\text{CD}} e^s)^2} + \frac{\epsilon_{\text{VI}} N_{\text{VI}} e^s}{(1 - \epsilon_{\text{VI}} e^s)^2}, \quad (76)$$

where $s < \min\{-\ln \epsilon_{\text{CD}}, -\ln \epsilon_{\text{VI}}\}$. According to the saddlepoint mass function [20, Eq. (1.13)], we obtain the PMF for $k > N_{\text{CD}} + N_{\text{VI}}$, which is the interior of the span of the support of $T_{\text{CD}}^{\text{cm}} + T_{\text{VI}}^{\text{cm}}$. For $k = N_{\text{CD}} + N_{\text{VI}}$, the probability can be simply obtained as $(1 - \epsilon_{\text{CD}})^{N_{\text{CD}}} (1 - \epsilon_{\text{VI}})^{N_{\text{VI}}}$.

APPENDIX C PROOF OF LEMMA 4

By rewriting Eq. (17), we obtain that

$$P_j = \varphi_j^{-c_3-1} (c_2 + (\tau_j)^{-c_3}). \quad (77)$$

P_j is a convex function of τ_j since $c_3 > 0$ and $\varphi_j > 0$. Thus, the conclusion in Lemma 4 is obtained by solving the following convex optimization problem:

$$\min_{\tau_{\text{PF1}}, \tau_{\text{PF2}}} \sum_{j \in \{\text{PF1}, \text{PF2}\}} \varphi_j^{-c_3-1} (c_2 + (\tau_j)^{-c_3}) \quad (78a)$$

$$\text{s.t. } \tau_{\text{PF1}} + \tau_{\text{PF2}} \leq \tau_{\text{PF}}. \quad (78b)$$

With the help of Karush–Kuhn–Tucker (KKT) conditions, the optimal solutions follows

$$\begin{cases} \lambda(\tau_{\text{PF1}} + \tau_{\text{PF2}} - \tau_{\text{PF}}) = 0, \\ -c_3 \varphi_j^{-c_3-1} \tau_j^{-c_3-1} + \lambda = 0, \quad j \in \{\text{PF1}, \text{PF2}\}, \end{cases} \quad (79)$$

where $\lambda > 0$ is the Lagrange multiplier. By solving equations (79), we obtain $\tau_{\text{PF1}} = \frac{\tau_{\text{PF}} \varphi_{\text{PF2}}}{\varphi_{\text{PF1}} + \varphi_{\text{PF2}}}$ and $\tau_{\text{PF2}} = \frac{\tau_{\text{PF}} \varphi_{\text{PF1}}}{\varphi_{\text{PF1}} + \varphi_{\text{PF2}}}$. The proof is completed.

APPENDIX D PROOF OF LEMMA 5

Let $G(\kappa) = \frac{\kappa}{\zeta_d(\kappa)}$. For $\zeta_d(\kappa)$ shown in Eq. (23), we obtain

$$\frac{dG(\kappa)}{d\kappa} = \frac{e^{\psi\kappa}(1 - \psi\kappa) - e^{\psi}}{\omega_0 (e^{\psi\kappa} - e^{\psi})^2}. \quad (80)$$

Since $\kappa \geq 1$, $\frac{dG(\kappa)}{d\kappa} \leq 0$ holds with $\psi \geq 1$. For $\zeta_d(\kappa)$ shown in Eq. (24), we have

$$\frac{dG(\kappa)}{d\kappa} = \frac{\omega_5 \omega_6 (1 - \omega_7) \kappa^{\omega_7} + \omega_5 \omega_8}{(\omega_5 (\omega_6 \kappa^{\omega_7} + \omega_8))^2}. \quad (81)$$

From this equation, we can find that $\omega_5 \omega_6 (1 - \omega_7) \kappa^{\omega_7}$ is decreasing with κ when $\omega_7 > 1$. Thus, the maximum value of $\omega_5 \omega_6 (1 - \omega_7) \kappa^{\omega_7}$ is achieved at $\kappa = 1$ since $\kappa \geq 1$, which is $\omega_5 \omega_6 (1 - \omega_7)$. Thus, if $\omega_5 \omega_6 (1 - \omega_7) + \omega_5 \omega_8 < 0$, i.e., $\omega_7 > 1 + \frac{\omega_8}{\omega_6}$, the maximum value of $\frac{dG(\kappa)}{d\kappa} < 0$.

For $\omega_7 \leq 1$, $\omega_5 \omega_6 (1 - \omega_7) \kappa^{\omega_7} \geq 0$. Thus, $\frac{dG(\kappa)}{d\kappa} > 0$.

REFERENCES

- [1] P. Popovski, F. Chiariotti, K. Huang, A. E. Kalør, M. Kountouris, N. Pappas, and B. Soret, "A perspective on time toward wireless 6G," *Proc. IEEE*, vol. 110, no. 8, pp. 1116–1146, Aug. 2022.
- [2] "Framework and overall objectives of the future development of IMT for 2030 and beyond," Recommendation ITU-R M.2160-0, Nov. 2023.
- [3] D. Gündüz, Z. Qin, I. E. Aguerri, H. S. Dhillon, Z. Yang, A. Yener, K. K. Wong, and C.-B. Chae, "Beyond transmitting bits: Context, semantics, and task-oriented communications," *IEEE J. Sel. Areas Commun.*, vol. 41, no. 1, pp. 5–41, Jan. 2023.
- [4] D. Gündüz, F. Chiariotti, K. Huang, A. E. Kalør, S. Kobus, and P. Popovski, "Timely and massive communication in 6G: Pragmatics, learning, and inference," *IEEE BITS Inf. Theory Mag.*, vol. 3, no. 1, pp. 27–40, Mar. 2023.
- [5] E. C. Strinati *et al.*, "Goal-oriented and semantic communication in 6G AI-native networks: The 6G-GOALS approach," in *2024 Joint European Conf. Netw. Commun. & 6G Summit (EuCNC/6G Summit)*, Jun. 2024.
- [6] M. Xu, W. C. Ng, W. Y. B. Lim, J. Kang, Z. Xiong, D. Niyato, Q. Yang, X. Shen, and C. Miao, "A full dive into realizing the edge-enabled metaverse: Visions, enabling technologies, and challenges," *IEEE Commun. Surveys Tuts.*, vol. 25, no. 1, pp. 656–700, 1st Quart., 2023.
- [7] "Feasibility Study on Localized Mobile Metaverse Services," V19.1.0, document 3GPP TR 22.856, Sep. 2023.
- [8] S. Suman, F. Chiariotti, Č. Stefanović, S. Došen, and P. Popovski, "Statistical characterization of closed-loop latency at the mobile edge," *IEEE Trans. Commun.*, vol. 71, no. 7, pp. 4391–4405, Jul. 2023.
- [9] D. Han, W. Chen, B. Bai, and Y. Fang, "Offloading optimization and bottleneck analysis for mobile cloud computing," *IEEE Transactions on Communications*, vol. 67, no. 9, pp. 6153–6167, Sept. 2019.
- [10] J. R. Lorch and A. J. Smith, "Improving dynamic voltage scaling algorithms with pace," *SIGMETRICS Perform. Eval. Rev.*, vol. 29, no. 1, p. 50–61, Jun. 2001.
- [11] E. Steinbach, S. Hirche, M. Ernst, F. Brandi, R. Chaudhari, J. Kammerl, and I. Victorias, "Haptic communications," *Proc. IEEE*, vol. 100, no. 4, pp. 937–956, Apr. 2012.
- [12] K. Antonakoglou, X. Xu, E. Steinbach, T. Mahmoodi, and M. Dohler, "Toward haptic communications over the 5G tactile internet," *IEEE Commun. Surveys Tuts.*, vol. 20, no. 4, pp. 3034–3059, 4th Quart., 2018.
- [13] P. Popovski, "Time, simultaneity, and causality in wireless networks with sensing and communications," *IEEE Open J. Commun. Soc.*, vol. 5, pp. 1693–1709, Mar. 2024.
- [14] J. Cao, X. Zhu, S. Sun, P. Popovski, S. Feng, and Y. Jiang, "Age of loop for wireless networked control system in the finite blocklength regime: Average, variance and outage probability," *IEEE Trans. Wireless Commun.*, vol. 22, no. 8, pp. 5306–5320, Aug. 2023.
- [15] L. Li, L. Yang, X. Guo, Y. Shi, H. Wang, W. Chen, and K. B. Letaief, "Delay analysis of wireless federated learning based on saddle point approximation and large deviation theory," *IEEE J. Sel. Areas Commun.*, vol. 39, no. 12, pp. 3772–3789, Dec. 2021.
- [16] B. Kizilkaya, C. She, G. Zhao, and M. A. Imran, "Task-oriented prediction and communication co-design for haptic communications," *IEEE Trans. Veh. Tech.*, vol. 72, no. 7, pp. 8987–9001, Jul. 2023.
- [17] D. Wen, P. Liu, G. Zhu, Y. Shi, J. Xu, Y. C. Eldar, and S. Cui, "Task-oriented sensing, computation, and communication integration for multi-device edge AI," *IEEE Trans. Wireless Commun.*, vol. 23, no. 3, pp. 2486–2502, Mar. 2024.
- [18] D. Van Huynh, S. R. Khosravirad, A. Masaracchia, O. A. Dobre, and T. Q. Duong, "Edge intelligence-based ultra-reliable and low-latency communications for digital twin-enabled metaverse," *IEEE Wireless Commun. Lett.*, vol. 11, no. 8, pp. 1733–1737, Aug. 2022.
- [19] P. M. de Sant Ana, N. Marchenko, P. Popovski, and B. Soret, "Age of loop for wireless networked control systems optimization," in *Proc. IEEE Int. Symp. Pers. Indoor Mob. Radio Commun. (PIMRC)*, Sept. 2021.
- [20] R. W. Butler, *Saddlepoint approximations with applications*. Cambridge, U.K.: Cambridge Univ. Press, 2007, vol. 22.
- [21] A. O. Kisilal, A. Lancho, G. Durisi, and E. G. Ström, "Efficient evaluation of the error probability for pilot-assisted URLLC with massive MIMO," *IEEE J. Sel. Areas Commun.*, vol. 41, no. 7, pp. 1969–1981, Jul. 2023.
- [22] L. Li, W. Chen, and K. B. Letaief, "On power-latency-throughput tradeoff of diversity enabled delay-bounded communications," in *Proc. IEEE Int. Conf. Commun. (ICC)*, Jun. 2023, pp. 2141–2146.
- [23] H. Cui, Y. Du, Q. Yang, Y. Shao, and S. C. Liew, "LLMind: Orchestrating AI and IoT with LLM for complex task execution," *IEEE Commun. Mag.*, early access, Sept. 27, 2024, doi: 10.1109/MCOM.002.2400106.
- [24] T. Kallehauge, P. Ramirez-Espinoza, A. E. Kalør, and P. Popovski, *Statistical Characterization of URLLC: Frequentist and Bayesian Approaches*. New York, NY, USA: John Wiley & Sons, Ltd, 2023, ch. 2, pp. 15–59.
- [25] L. Li, W. Chen, and K. B. Letaief, "Simple bounds on delay-constrained capacity and delay-violation probability of joint queue and channel-aware wireless transmissions," *IEEE Trans. Wireless Commun.*, vol. 22, no. 4, pp. 2744–2759, Apr. 2023.
- [26] L. Li, W. Chen, and K. B. Letaief, "Fitting Empowered Cross-Layer Scheduling for Real-Time Wireless Communications," accepted by *Proc. IEEE Int. Conf. Commun. (ICC)*, 2024.
- [27] M. Bennis, M. Debbah, and H. V. Poor, "Ultrareliable and low-latency wireless communication: Tail, risk, and scale," *Proc. IEEE*, vol. 106, no. 10, pp. 1834–1853, Oct. 2018.
- [28] C.-F. Liu, M. Bennis, M. Debbah, and H. V. Poor, "Dynamic task offloading and resource allocation for ultra-reliable low-latency edge computing," *IEEE Trans. Commun.*, vol. 67, no. 6, pp. 4132–4150, Jun. 2019.
- [29] R. D. Yates, Y. Sun, D. R. Brown, S. K. Kaul, E. Modiano, and S. Ulukus, "Age of information: An introduction and survey," *IEEE J. Sel. Areas Commun.*, vol. 39, no. 5, pp. 1183–1210, May 2021.
- [30] A. Maatouk, S. Kriouile, M. Assaad, and A. Ephremides, "The age of incorrect information: A new performance metric for status updates," *IEEE/ACM Trans. Netw.*, vol. 28, no. 5, pp. 2215–2228, Oct. 2020.
- [31] L. Li, W. Chen, P. Popovski, and K. B. Letaief, "Reliability-Latency-Rate Tradeoff in Low-Latency Communications with Finite-Blocklength Coding," accepted, *IEEE Trans. Inf. Theory*, 2024.
- [32] L. Li, W. Chen, and K. B. Letaief, "Ultra-reliable and low latency wireless communications with burst traffics: A large deviation method," in *Proc. IEEE Global Commun. Conf. (GLOBECOM)*, Dec. 2021.
- [33] L. Li, W. Chen, and K. B. Letaief, "Wireless communications with hard delay constraints: Cross-layer scheduling with its performance analysis," *IEEE Internet Things J.*, vol. 11, no. 20, pp. 32540–32556, Oct. 2024.
- [34] X. Li, C. You, S. Andreev, Y. Gong, and K. Huang, "Wirelessly powered crowd sensing: Joint power transfer, sensing, compression, and

- transmission," *IEEE J. Sel. Areas Commun.*, vol. 37, no. 2, pp. 391–406, Feb. 2019.
- [35] T. T. Nguyen, V. N. Ha, L. B. Le, and R. Schober, "Joint data compression and computation offloading in hierarchical fog-cloud systems," *IEEE Trans. Wireless Commun.*, vol. 19, no. 1, pp. 293–309, Jan. 2020.
- [36] Y. Zhang and Y. K. Kwok, "Saddlepoint approximations to tail expectations under non-gaussian base distributions: option pricing applications," *J. Appl. Stat.*, vol. 47, no. 11, pp. 1936–1956, 2020.
- [37] "Ternary Search," *Geeksforgeeks*. [Online]. Available: <https://www.geeksforgeeks.org/ternary-search/>.